

pH Dependence of Zika Membrane Fusion Kinetics Reveals an Off-Pathway State

Robert J. Rawle,^{†,#} Elizabeth R. Webster,^{‡,#} Marta Jelen,[†] Peter M. Kasson,^{*,†,§} and Steven G. Boxer^{*,‡}

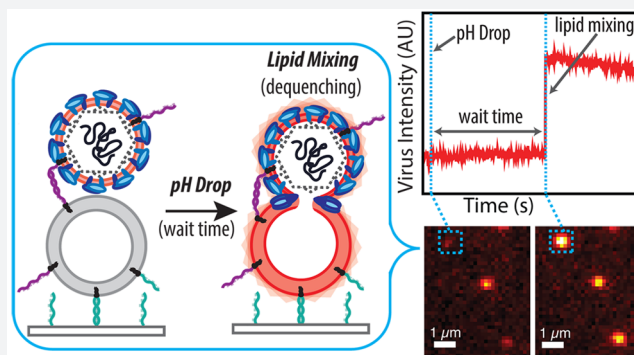
[†]Departments of Molecular Physiology and Biological Physics and of Biomedical Engineering, University of Virginia, Charlottesville, Virginia 22908, United States

[‡]Department of Chemistry, Stanford University, Stanford, California 94305, United States

[§]Science for Life Laboratory, Department of Cell and Molecular Biology, Uppsala University, Uppsala, Sweden 75124

Supporting Information

ABSTRACT: The recent spread of Zika virus stimulated extensive research on its structure, pathogenesis, and immunology, but mechanistic study of entry has lagged behind, in part due to the lack of a defined reconstituted system. Here, we report Zika membrane fusion measured using a platform that bypasses these barriers, enabling observation of single-virus fusion kinetics without receptor reconstitution. Surprisingly, target membrane binding and low pH are sufficient to trigger viral hemifusion to liposomes containing only neutral lipids. Second, although the extent of hemifusion strongly depends on pH, hemifusion rates are relatively insensitive to pH. Kinetic analysis shows that an off-pathway state is required to capture this pH-dependence and suggests this may be related to viral inactivation. Our surrogate-receptor approach thus yields new understanding of flaviviral entry mechanisms and should be applicable to many emerging viruses.



INTRODUCTION

Zika virus, an enveloped flavivirus, has recently emerged as a global health concern, causing febrile illness and congenital abnormalities.^{1–4} It is a positive-sense, single-stranded RNA virus that is primarily transmitted to humans from *Aedes* mosquitoes. Because Zika has only recently received much scientific study, its entry and fusion processes remain largely uncharacterized but are important both for scientific understanding and as possible targets for therapeutic intervention.

Currently, the entry and fusion of Zika are mostly understood by analogy to closely related flaviviruses such as dengue virus and West Nile virus. To infect a host cell, these viruses first bind to a receptor on the host cell surface. The virus is then internalized by endocytosis, and, as the endosome matures, its internal pH drops. This triggers a dramatic rearrangement in the viral E-proteins, which mediate fusion with the endosomal membrane, allowing the viral RNA to enter the cell.^{5–8} Several factors in addition to low pH, such as endosomal lipid composition and the extent of viral maturity,^{9–12} affect the fusion process and may play a regulatory or triggering role for some or all flaviviruses. The mechanism of fusion continues to be the subject of investigation, and the level of detail at which fusion mechanisms are conserved among flaviviruses is unknown.^{13–15}

Mechanistic studies of Zika viral fusion thus have the potential to inform Zika biology as well as shed light on the degree of mechanistic conservation among flaviviruses. Critical questions include whether pH is sufficient to trigger fusion or merely one of several required factors, the pH range at which fusion occurs, and what other factors may be required for efficient fusion. Single-virus studies on the fusion of Zika virus to model membranes offer a means to probe these mechanisms in a controlled fashion and selectively reconstitute host components. Although there have been several receptors proposed for Zika virus (e.g., AXL), there is little consensus as to which, if any, is the key receptor for binding and what role it may play in triggering fusion.^{16–20} While live-cell measurements can permit tracing of individual virions through the entry process, precise measurement of fusion conditions is challenging, and the ability to precisely perturb these conditions even more so. We and others have measured the fusion of infectious virus to synthetic target membranes, which permits exquisite control over the timing of fusion triggering, target membrane composition, and other soluble factors for fusion.^{21–25} This approach enables richer mechanistic understanding, as evidenced by a

Received: July 24, 2018

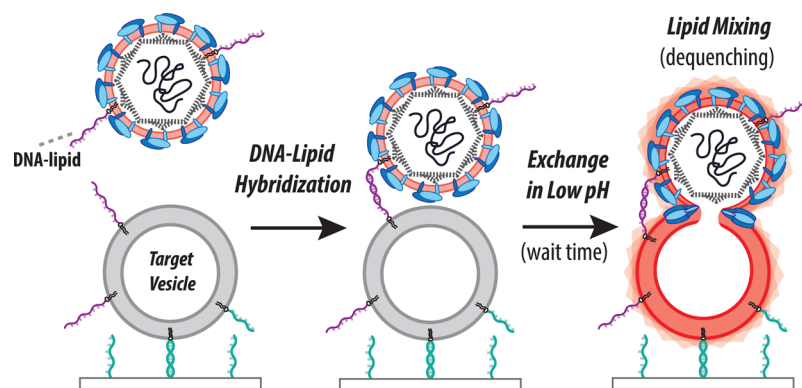


Figure 1. Schema of single virus fusion assay. Zika virus displays a low number of DNA–lipids and is fluorescently labeled with a self-quenched concentration of dye-labeled lipid (light pink). The target vesicles are tethered to a DNA-functionalized glass coverslip inside a microfluidic device by DNA–lipid hybridization (teal, sequence B–B’ orthogonal to purple DNA strands). Hybridization of viral and target DNA–lipids (purple, Sequence A–A’) binds the virus to the vesicle. Low pH buffer is exchanged into the microfluidic device to trigger fusion, which is observed by fluorescence dequenching due to lipid mixing between virus and target.

number of single virus binding and fusion studies, including West Nile virus.^{21,26–29} Similarly, single-virus fusion kinetics yield a window into the fusion mechanism, in particular shedding light on mechanistic heterogeneity and the family of reactions required for fusion. This has been pursued fruitfully for other enveloped viruses^{27,30–33} as well as nonviral systems.^{34,35}

Here, we use an approach to single-virus measurement of Zika fusion that permits deconvolution of receptor/membrane binding from fusion. We have previously shown for influenza virus that tethering virions to target membranes using complementary DNA–lipid hybrids in the absence of native receptor can substitute for receptor binding.³⁰ In the case of influenza, where pH is the only trigger for fusion, we observed no measurable difference between the fusion (lipid mixing) kinetics of influenza bound by DNA–lipids or by its native receptor. We now leverage this approach to study the fusion of Zika virus, where a clear cellular receptor is not known. The driving hypothesis of our work is that if DNA–lipid tethering of Zika virus results in pH-triggered fusion, the fusion mechanisms will be at least informative of the mechanisms of fusion following receptor-mediated binding if not identical to those mechanisms. We show that fusion can indeed be triggered by pH alone and that negatively charged lipids are not required for Zika fusion. Our data suggest that if the pH range of fusion is considered alone, Zika virus hemifusion could occur in early endosomes and hemifusion efficiency would be further enhanced as the endosome matures. Additionally, we observe that while the efficiency of fusion is pH-sensitive, overall rates of fusion are relatively insensitive to pH (although there is a shift from rates at pH ~6 to pH ~5, which we discuss). We use kinetic modeling to analyze these results and demonstrate that an off-pathway state is required to reproduce our waiting-time distributions in any simple kinetic model. This off-pathway state represents one form of viral inactivation and is thus an important consideration for design and evaluation of fusion inhibitors.

RESULTS AND DISCUSSION

Single-virus measurements of Zika fusion kinetics via fluorescence microscopy require specifically labeled virus bound to target membranes. We performed this using virus labeled with a self-quenched concentration of Texas Red-DHPE bound to vesicles using DNA–lipid conjugates as schematized in

Figure 1 and described in the Materials and Methods. Specific labeling was confirmed via immunofluorescence and immunoblotting (Figures S1 and S2); approximately 65% of fluorescently labeled particles were immunopositive for Zika E-protein. To examine the effect of labeling on viral integrity, labeled Zika virions were also confirmed via RT-qPCR to contain viral RNA (SI Appendix, Section 1.8), indicating that the labeling process did not grossly disrupt virions. Binding of labeled Zika virions to target vesicles immobilized within a microfluidic flow cell was highly specific, as negligible binding was observed when noncomplementary DNA sequences were used (Figure S4).

Single-virus Zika fusion kinetics were measured by triggering fusion using a low-pH buffer exchange over a 1–2 s interval, calibrated using pH-dependent fluorescence of target vesicles containing Oregon Green dye. For each labeled virion, the waiting time between pH drop and the onset of lipid mixing (a marker of hemifusion as lipid-conjugated dye is transferred from virus to vesicle and thus diluted) or, conversely, a failure to achieve lipid mixing was recorded. Representative images and fusion traces are shown in Figure 2. Waiting times for many virions were then compiled into a cumulative distribution function (CDF) (Figure 3A,B). The shape and time scale of the CDF contain information about the kinetically resolvable steps in the hemifusion process, which can be examined by kinetic modeling. CDFs are preferred over histograms to present waiting time data because they do not require binning time data, which can produce artifacts.³⁶

To examine the role of pH in Zika virus fusion, we performed single virus lipid mixing experiments across a range of pH values designed to mimic endosomal pH values through most of the endocytic pathway (Figure 3A,B). We observed lipid mixing across the entire range of pH values tested, suggesting that the pH becomes permissive for Zika virions quite early during endosomal maturation and continues through late endosome to lysosome maturation. From pH 6.9 to pH 4.6, hemifusion efficiency increased approximately 3-fold in a roughly linear fashion (Figure 3A). The maximum efficiency of Zika virus lipid mixing is comparable to similar single virus fusion experiments with West Nile virus.²⁶ By way of comparison, dengue virus fusion largely occurs in late endosomes, although this may be determined by lipidic factors.^{12,25,37} We hypothesize that negatively charged lipids, commonly found in late

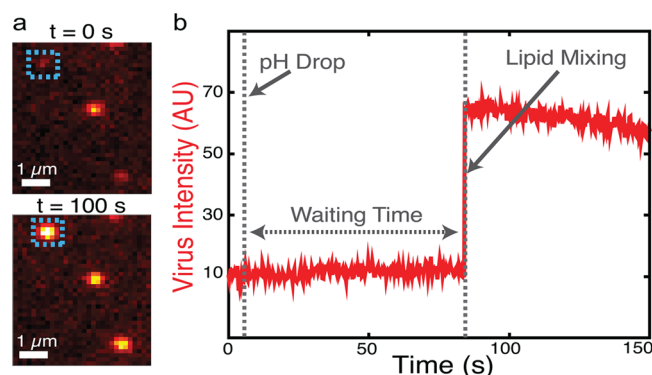


Figure 2. Single-virus fusion observed via fluorescence dequenching. (a) Example fluorescence micrographs of individual Zika virions (colored spots) bound to target vesicles (not visualized). At $t = 0$ (top) the virions' fluorescence is self-quenched but detectable as a dim spot. After low pH buffer exchange, 2 of 3 particles in the field of view exhibit dequenching due to lipid mixing after 100 s (bottom). (b) The fluorescence intensity trace of the virion boxed in A shows a sudden jump to higher fluorescence due to lipid mixing followed by photobleaching. The hemifusion wait time is defined as the time between pH drop and the onset of lipid mixing.

endosomes, function by either promoting viral attachment or enhancing an already fusion-competent virus; however, further work is necessary to explore the effect of lipid composition on fusion kinetics of Zika virus. While our data do not eliminate the possibility of additional cofactors regulating or enhancing Zika fusion within the endosome, low pH is sufficient to trigger lipid mixing events when Zika virus is bound to model membranes. We also observed a low ($\sim 2\text{--}3\%$) efficiency of lipid mixing events at pH 7.4 that was significantly less than all lower pH values ($p < 0.001$ minimum) (Figure S6). This may suggest a low but nonzero probability of fusion at neutral pH if the virion is bound near a target membrane, which is further described in the Supporting Information (SI Appendix, section 2.1). As a control, when vesicles are tethered instead of virus, no fusion events are observed within the pH range of 7.4–4.6, and thus this behavior is specific to the presence of Zika virus.

In contrast to hemifusion efficiencies, hemifusion rates were relatively independent of pH (Figure 3B). Rates of lipid mixing

increase slightly at lower pH values, but this effect was small compared to the magnitude of pH change: over a range where $[\text{H}^+]$ varied 200-fold, the $t_{1/2}$ for lipid mixing varied by no more than 2-fold. Therefore, while low pH is sufficient to trigger Zika virus, the rates of lipid mixing are largely insensitive to pH. Prior studies on other flaviviruses have shown that E-protein activation is pH sensitive.^{26,38–43} Our data would indicate that such an activation step, although potentially pH-driven, is not rate-limiting for Zika fusion at pH < 5.8. As discussed below, this observation provides important constraints to the kinetic mechanism of fusion.

Kinetic Modeling of Zika Virus Hemifusion Data Suggests an Off-Pathway State. To analyze the mechanistic implications of our measurements of Zika hemifusion, we fit a series of kinetic models to the pH-dependent hemifusion data. We begin with simple models from chemical kinetics that assume well-mixed states with Markovian behavior; models that explicitly treat spatial patterns of fusion protein activation will be discussed later. These simple models assume that the underlying mechanism of fusion is conserved in pH-triggered fusion. It is apparent from gross examination of the waiting-time distributions (Figure 3) that overall lipid-mixing rates are roughly independent of pH at low pH but slower at high pH. This behavior requires at least two kinetic steps in a minimal model (1) a pH-independent step that is rate-limiting at low pH values, and (2) a pH-dependent step that is rate-limiting at higher pH values (5.8–7.4). This then leads to the following two-step minimal mechanism:



where B denotes bound virus, A denotes pH-activated virus in the membrane-bound state, and F denotes hemifused virus. For clarity we omit the state of the virus prior to membrane binding, as our experimental observation begins with virus bound to the target vesicle prior to pH drop. Therefore, we treat state B as the starting state of all viruses upon target binding. The final step leading to state F is treated as irreversible and is assigned as the pH-independent step. The pH-dependent step, state B to A, is treated as reversible, but $k_{\text{AB}} \ll k_{\text{BA}} [\text{H}^+]$ at all pH values tested, or a lag phase would have been observed in the CDF data. The pH-dependent transition has been postulated

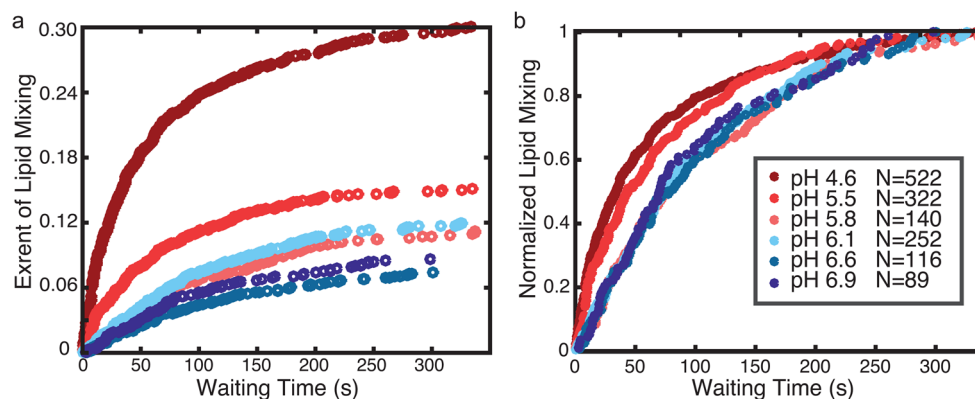


Figure 3. Zika virus hemifusion efficiency is sensitive to pH but rates are not. Plotted are cumulative distribution functions compiled from single-virus lipid-mixing wait times collected at different pH values and either normalized to fraction of total E-protein-positive particles (a) or normalized by the maximum observed fraction of lipid mixing at each pH value (b). Across the pH range, efficiency changes ~ 3 fold: 333/1748 particles at pH 4.6, 145/1514 particles at pH 5.5, 95/1346 particles at pH 5.8, 186/2447 particles at pH 6.1, 68/1447 particles at pH 6.6, and 63/1145 particles at pH 6.9. Kinetic data were compiled from 29 independent fusion streams and replicated with an independent viral preparation. Fraction of total E-protein-positive particles was calculated using mean values measured via immunofluorescence assay (IFA) as described in Supporting Information.

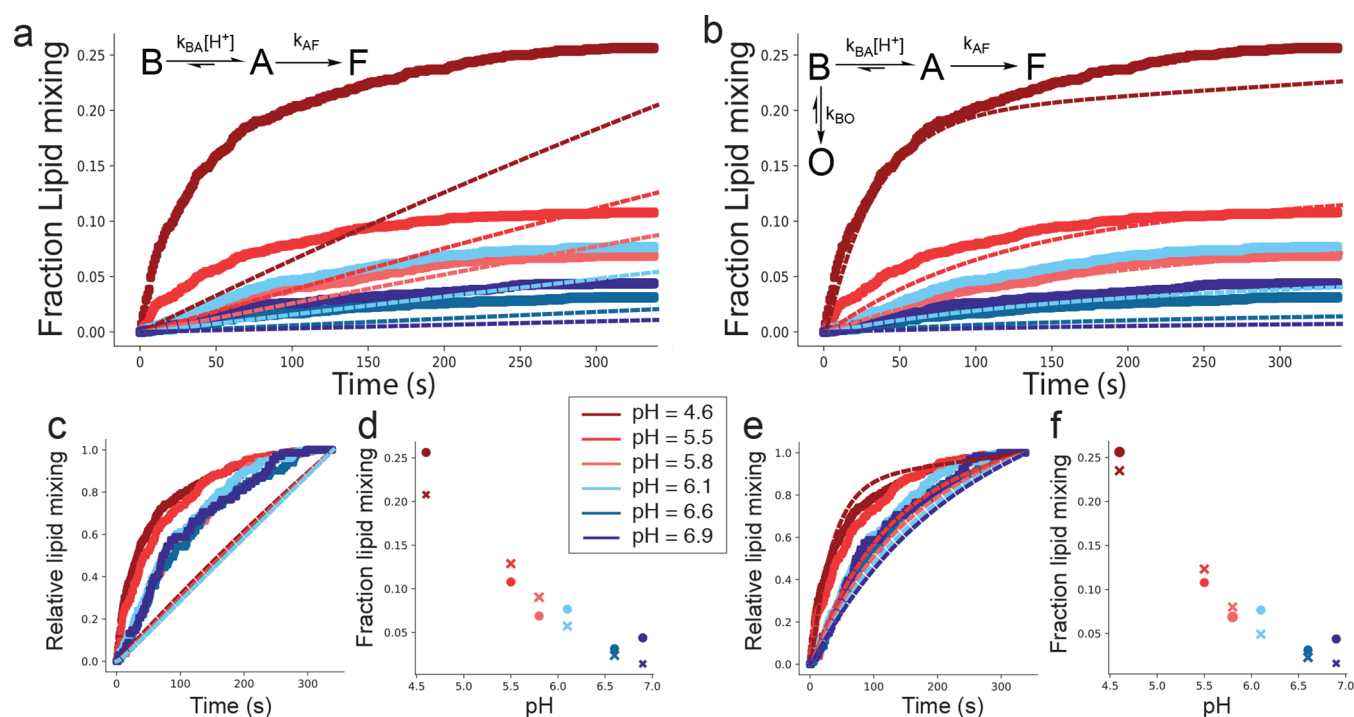
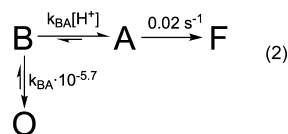


Figure 4. An off-pathway model is necessary to capture pH-dependent fusion kinetics. Plotted in panels A–B are lipid-mixing kinetic curves calculated from a linear model (a) and an off-pathway model (b) in thin lines, compared to observed single-virus fusion data at multiple pH values (thick lines). Kinetics are further visualized by normalizing all efficiencies to one (c and e for linear and off-pathway models), and efficiencies are estimated as the extent of lipid mixing at the end of the experiment (d, f). The linear model reproduces the lipid-mixing efficiency trends but does so at the expense of curve shape. The best-fit rate constants were $k_{BA} = 5.4 \times 10^4 \text{ M}^{-1} \text{ s}^{-1}$, $k_{BO} = 6.0 \times 10^{-3} \text{ s}^{-1}$, $k_{AB} = 0.29 \text{ s}^{-1}$, $k_{AF} = 0.088 \text{ s}^{-1}$, and $k_{OB} = 1.3 \times 10^{-4} \text{ s}^{-1}$.

to be related to the protonation of key histidines leading to a conformational shift.^{40,43} The rate constant of the pH-independent step, k_{AF} , is estimated at 0.02 s^{-1} by approximating the CDF at pH 4.6 (where the pH-independent step should be rate-limiting) as a single exponential and solving the resulting equation.

This two-step mechanism can reasonably describe the hemifusion rates alone (Figure S7), but cannot successfully fit both rates and hemifusion efficiencies (Figure 4 and Figure S12). Indeed, any linear mechanism of this form cannot fit both the observed rates and efficiencies, even if additional states are added (compare Figure S12 and Figures S7–S9). A linear mechanism can only produce an efficiency less than one by generating kinetic curves that have not yet plateaued at the end of the experiment (Figure S12 and Figure S7). This agrees poorly with the observed CDFs as well as validation experiments where we extended the measurement window and did not measure a substantial increase in efficiency.

In order to capture both the observed rates and efficiency data, we found it necessary to include an off-pathway state in the reaction mechanism (eq 2). In this case, the on-pathway steps largely govern the rates, but partitioning between the on- and off-pathway states determines the final efficiencies.



Rate constants for conversion to and from the off-pathway state O were estimated as follows. In this model, at pH values where $k_{BA} [\text{H}^+] \gg k_{BO}$, the relative efficiency approaches 1; conversely, when $k_{BA} [\text{H}^+] \ll k_{BO}$, the efficiency approaches 0.

When the two are equal, the final efficiency is 0.5. By roughly treating our efficiency data (extents from Figure 3A) as linear with respect to pH, we estimated the off-pathway state should be half populated around pH 5.7 (Figure S11). Consequently, we set $k_{BO} = k_{BA} \times 10^{-5.7}$. Because our efficiency data is pH-dependent, the off-pathway state must occur in competition with the pH-dependent step; otherwise no pH dependence would be observed. For the same reason, transition rates to the off-pathway state also cannot be first-order with respect to $[\text{H}^+]$. Our initial analyses approximate conversion to the off-pathway state as irreversible; however this model does not rule out possibility for a slow return from the off-pathway state. Indeed, unconstrained fits presented in Figure 4 show $0 < k_{OB} \ll k_{BO}$. As noted above, state B is assumed to be the starting state of the model following virus binding. The off-pathway state depends on close proximity to a target membrane; otherwise, the native state of the virus prior to membrane binding would largely be in this off-pathway state and fusion would not be observed.

Using the model in eq 2, we performed a one parameter fit to our lipid mixing data, only allowing k_{BA} to vary (Figure S12). Despite the simplified nature of this model, we found better agreement with the general features of our data—pH-dependent efficiencies with only minimal change in hemifusion rates.

However, the lipid mixing efficiencies obtained via this model were essentially linear with respect to pH and approached zero at high pH. In contrast, the observed efficiencies approached a limiting value of 2–3% at pH 7.4. As low pH has been shown to be necessary for efficient infection by Zika virus,⁴⁴ we further concentrated on the pH-dependent lipid mixing process and corrected the cumulative distribution functions at all

other pH values by subtracting the pH 7.4 CDF (Figure S13). Using these corrected lipid-mixing curves, we performed fits of the models in eqs 1 and 2, allowing all parameters to vary freely fitting all pH values simultaneously. We observed that an off-pathway model was still required (Figure 4) and that the background subtraction improved the fitted efficiencies (compare Figure S12 and Figure 4). This suggests that an off-pathway state is required to fit our lipid mixing data with any simple kinetic model.

Cellular Automaton Models of Fusion Kinetics. Because many viral fusion processes are known to require multiple fusion proteins, cellular automaton models have been developed to incorporate protein spatial arrangement and activation into the analysis of single-virus fusion traces.^{26,33,45} These models also incorporate structural and biochemical information to hypothesize the molecular identities of intermediate states in the kinetic schemes employed. We therefore implemented a cellular automaton model that was previously used to analyze West Nile virus fusion,²⁶ consisting of four structural states in a linear reaction scheme, and used it to analyze our pH-dependent Zika virus fusion data in a fashion analogous to the simpler models above.

To determine whether the geometrical constraints in the simulation model could compensate for the requirement of an off-pathway state in the simple kinetic model (eq 2), we implemented a number of kinetic schemes within the cellular automaton framework and fit them to our data. Parameterization of the model is described in the [Supporting Information \(SI Appendix, Section S.3\)](#) and was performed analogously to that previously reported for West Nile virus, but with careful treatment of pH pre-equilibration for multi-pH experiments. None of the linear models tested were able to fit the Zika virus fusion data (Figures S14 and S15). However, addition of an off-pathway state in the cellular automaton model (Figure S15) analogous to eq 2 above resulted in a fit approximately similar in quality to the best-fit parameters for eq 2. Whether a simple or more complex kinetic scheme is used, we conclude that an off-pathway state is needed to capture both the efficiency and rates of Zika virus hemifusion as pH is varied.

According to the structural hypotheses encoded in prior models of West Nile virus,²⁶ our related model for Zika suggests that E-protein monomers could adopt an off-pathway conformation following insertion into the target membrane. This transition is either slowly reversible or irreversible on the time-scales of fusion. There are currently insufficient biochemical data on Zika virus to definitively assign structural identities to the states in our model, so this remains speculation. If we accept prior biochemical analyses and hypotheses regarding related viruses, this off-pathway state would be closely related to viral inactivation, although our model requires the off-pathway state to depend on the presence of target membranes and thus may be distinct from additional slow inactivation of flaviviruses in solution.^{46,47}

Finally, we note that both the simple kinetic and cellular automaton models have a similar categorical shortcoming: They both predict that lipid-mixing efficiency should be very sensitive to the time delay between virus binding to the target membrane and pH drop, which we do not observe. In our experimental data, viruses bound to target membranes showed similar kinetic behavior whether bound for <10 or >20 min prior to the pH drop (Figure S16). This indicates that, although an off-pathway state is required, neither model is complete, and suggests an avenue for follow-up investigation.

CONCLUSION

Using DNA–lipids as surrogate viral receptors permits the study of Zika virus fusion mechanisms distinct from viral binding and even without definitive identification of the natural receptor. Measuring single-virus fusion events in this manner, we have established that pH is sufficient to trigger fusion of prebound virus to synthetic target membranes. Viral hemifusion can occur in a pH range consistent with early endosomes but increases in efficiency at lower pH values. This suggests that the pH of late endosomes and lysosomes is also compatible with Zika viral fusion, although other factors in different endocytic compartments such as lipid composition changes and protease activity may act to promote or inhibit fusion in different compartments. Prior work has tracked dengue and West Nile virions trafficking in live cells and proposed that those viruses fuse in late endosomes,^{12,25,37,48} and this is likely the case for Zika as well.

Strikingly, the rates of Zika hemifusion were largely insensitive to pH, suggesting that the rate-limiting step of hemifusion must be pH-independent below approximately pH 6. This finding implies that conformational extension of the viral E-protein to permit fusion, demonstrated to be a pH-dependent process for closely related flaviviruses,^{26,38,49,50} is not rate-limiting in this pH range. We have deliberately avoided assigning specific structural features to states in our kinetic models, but our modified implementation of prior cellular automaton models used for West Nile data to fit Zika viral fusion kinetics raises the hypothesis that the off-pathway state we detect in Zika fusion may occur after E-protein extension and insertion into the target membrane. Speculatively, this could represent an aggregation, misfolding, or similar state of the E-protein which contributes to inactivation.

In addition to low pH, other factors have been implicated in regulating flavivirus fusion, including endosomal lipid composition, temperature, and extent of viral maturation.^{9,12} Our results suggest that pH is sufficient to trigger Zika virus fusion, but they do not exclude the possibility of other endosomal factors influencing the fusion process or enhancing fusion efficiency. Our single virus fusion platform enables future examination of how these and other factors affect Zika virus fusion. We anticipate that this platform using DNA–lipids as surrogate receptors will also facilitate the study of single-virus fusion by other enveloped viruses with unknown or difficult-to-isolate native receptors.

MATERIALS AND METHODS

Materials. Dioleoylphosphatidylethanolamine (DOPE), palmitoyl oleoylphosphatidylcholine (POPC), and cholesterol were purchased from Avanti Polar Lipids (Alabaster, AL). Texas Red-1,2-dihexadecanoyl-*sn*-glycero-3-phosphoethanolamine (TR-DHPE), Oregon Green-1,2-dihexadecanoyl-*sn*-glycero-3-phosphoethanolamine (OG-DHPE), goat anti-mouse IgG (H + L) secondary antibody, Alexa Fluor 488 and anti-flavivirus group antigen, and clone: D1-4G2-4-15, EMD Millipore were purchased from Thermo Fisher Scientific (Waltham, MA). IRDye 680RD goat anti-mouse IgG (H + L) 0.5 mg/mL was generously supplied by the Bertozzi lab (Stanford University). PCR primers were ordered from the Stanford PAN Facility, (SI Appendix, Table S2). Chloroform, methanol, and buffer salts were obtained from Fisher Scientific (Pittsburgh, PA) and Sigma-Aldrich (St. Louis, MO). 11-Azidoundecyltrimethoxysilane was obtained from Sikemia (Clapiers, France).

Polydimethylsiloxane (PDMS) was obtained from Ellsworth Adhesives (Hayward, CA). Tridecafluoro-1,1,2,2-tetrahydrooctyltrichlorosilane was obtained from Gelest (Morrisville, PA). 1,1',1''-Tris(1*H*-1,2,3-triazol-4-yl-1-acetic acid ethyl ester) trimethylamine (TTMA) ligand was a generous gift from Professor Christopher Chidsey at Stanford University. Ethynyl phosphonic acid was synthesized as previously described.⁵¹ Zika virus is a BSL-2 agent and was handled following an approved administrative biosafety panel protocol at Stanford University. No other unexpected or unusually high safety hazards were encountered with this work.

Buffers. The following buffers were used. Reaction buffer (RB) = 10 mM NaH₂PO₄, 90 mM sodium citrate, 150 mM NaCl, pH 7.4. Fusion buffer (FB) = 10 mM NaH₂PO₄, 90 mM sodium citrate, 150 mM NaCl, pH as indicated. HB buffer = 20 mM Hepes, 150 mM NaCl, pH 7.2. sucrose cushion = 20% m/v sucrose, 20 mM Hepes, 150 mM NaCl, pH 7.3. We found it necessary to charcoal filter our sucrose solutions, which contained contaminant green fluorescence present from the manufacturer and which otherwise made it impossible to perform our single-molecule DNA–lipid incorporation measurements. As a cautionary note to other researchers, this charcoal filtration can substantially alter the pH of the sucrose cushion, unless it is appropriately buffered.

Microscopy. All epifluorescence micrographs and videos were acquired with a Nikon Ti-U microscope using a 100× oil immersion objective, NA = 1.49 (Nikon Instruments, Melville, NY), with a Spectra-X LED Light Engine (Lumencor, Beaverton, OR) as an excitation light source, and additional excitation/emission filter wheels (SI Appendix, Supporting Methods S1.9). Images were recorded with an Andor iXon 897 EMCCD camera (Andor Technologies, Belfast, UK) using 16-bit image settings and were captured with Metamorph software (Molecular Devices, Sunnyvale, CA). See Supporting Information (SI Appendix) for additional microscope details.

Viral Growth. Zika Virus (DAKAR41524) was grown in Vero cells according to an adaptation of a standard protocol for dengue virus.⁵² Cells at approximately 80% confluence were inoculated at a multiplicity of infection of approximately 0.05, grown in DMEM media with 2% fetal bovine serum, and the supernatant was harvested at 96 and 120 h after incubation in a tissue culture incubator at 37 °C, 5% CO₂. Gross cellular debris was removed by centrifugation at 4000 rcf, 4 °C for 10 min, and the sample was concentrated 20× by centrifugation in 30 kDa-cutoff spin concentrators and frozen at –80 °C until purification. We observed that this protocol maintained viral infectivity better than freezing unconcentrated supernatant in 23% fetal bovine serum until purification.

Viral Purification and Labeling. Zika virus was thawed on ice overnight before ultracentrifugation through a 20% sucrose cushion at 100000g for 3 h at 4 °C. The supernatant was discarded, and the pellet was resuspended by extensive pipetting in 100 μL of HB. To prepare the dye labeling solution, a 400 μL solution of 13.5 μM Tx-Red DHPE in HB with 2.5% ethanol was sonicated at 55 °C for 20 min then cooled to room temperature. We found it necessary to heat/sonicate the dye labeling solution prior to virus addition. This dispersed dye aggregates that would otherwise be copurified with viral particles. The resuspended virus was added to the dye solution (yielding a 10 μM Tx-Red DHPE solution) and gently rocked at 25 °C for 2 h. To purify away free dye, the labeled virus mixture underwent ultracentrifugation through a 20% sucrose cushion at 100000g for 3 h at 4 °C. The pellet was

resuspended in fresh 100 μL HB. This labeled virus suspension was stored at 4 °C and used in lipid mixing assays within several days. A self-quenching concentration of dye is required to accurately quantitate lipid mixing between virus and 100 nm vesicles. This labeling procedure is similar to those we and others have used to label other enveloped viruses, and the dye concentrations used in these experiments are lower than those previously found not to perturb West Nile and Kunjin virus infectivity.²⁶ Additionally, a 2-fold increase in the TR-DHPE dye added did not alter the measured lipid-mixing efficiency (Figure S5).

DNA–Lipid Incorporation into Zika Virions. The number of fluorescently labeled particles was estimated by adsorption of a fixed volume of viral suspension to a cleaned glass coverslip and counted using fluorescence microscopy. DNA–lipids were added at a ratio of 10 μM DNA–lipid to an estimated 1 pM of viral particles and allowed to incubate for 30 min at 24 °C to ensure all virions incorporated DNA–lipid. Single-step photobleaching was performed on particles with DNA–lipids conjugated to Alexa 488 (Sequence X, Table S1) to determine the number of DNA–lipids incorporated into each particle. The median number of DNA–lipids per virion was two (Figure S3). DNA sequence A and A' were utilized for viral binding and fusion because they increased tethering speed and density of bound virions per field of view (FOV). The increased binding speed of DNA sequence A and A' as compared to B and B' is likely a result of the former being a non-fully overlapping sequence, which leads to faster tethering as characterized in earlier work.³⁴

Lipid-Mixing Assay. Lipid-mixing assays were performed as previously described³⁰ and (Figure 1). In brief, target membranes, ~100 nm diameter lipid vesicles displaying DNA–lipid sequences A' and B (SI Table 1), were tethered to glass slides functionalized with sequence B' inside of a microfluidic flow cell in the presence of RB. Excess vesicles were rinsed from the flow cell with RB. An estimated 10 pmol of labeled virions containing DNA-lipid sequence A was added to the flow cell, and the cell was then rinsed with RB after 2–5 min to remove excess unbound virus. Fluorescence microscopy was used to collect a stream of images for 1200 frames at a frame rate of 3.47 frames/s. After the start of the stream, low pH buffer (FB pH 4.6–6.9) was immediately exchanged into the chamber and the flow was started. Vesicles with a pH indicator (2 mol % OG-DHPE) were used to calibrate the exchange time of the low pH buffer (FB pH 5.1) (1–2 s).³⁰ The time between introduction of low pH to the field of view (FOV) and dequenching events was then analyzed using Matlab (source code available from <https://github.com/kassonlab>).

Kinetic Modeling. Construction and fitting of kinetic models to the lipid mixing data were performed using Matlab and Python code available from <https://github.com/kassonlab>. For each kinetic model, matrix exponentials were used to solve the system of coupled ordinary differential equations and calculate the fraction of virions that have undergone lipid mixing at discrete time points between 0 and 340 s, corresponding to the cumulative distribution function (CDF) curves compiled from our experimental data at each waiting time after pH drop ($t = 0$). Additionally, to account for the time period between virus binding to target vesicles and pH drop (~10 min), the kinetic model was run for 10 min at pH 7.4, and this was used as the starting state at $t = 0$. All viruses were defined to be in the first state at $t = -10$ min (State B in the scheme shown in eq 2).

Kinetic model parameters were fit to the data across all pH values simultaneously using a maximum-likelihood procedure as follows. The probability density function (PDF) for lipid mixing at a particular pH is expressed as

$$f(x; k, \text{pH}) = \begin{cases} \pi(k, \text{pH})f_{\text{hemi}}(x; k, \text{pH}) & x_{\text{hemi}} \\ 1 - \pi(k, \text{pH}) & x_{\text{not}} \end{cases} \quad (3)$$

where k is the set of rate constants in the model, π is the hemifusion efficiency, x_{hemi} is the hemifusion wait time of a virus that underwent lipid mixing, x_{not} is a virus observed not to undergo lipid mixing, and f_{hemi} is the PDF of hemifusion wait times. f_{hemi} was calculated as the numerical derivative of the solution to the kinetic master equation. This then leads to the log likelihood expression:

$$\log L(x; k, \text{pH}) = \sum_x (\log f(x_{\text{hemi}}; k, \text{pH})) + N_{\text{hemi}} \log \pi(k, \text{pH}) + N_{\text{not}} \log(1 - \pi(k, \text{pH})) \quad (4)$$

where x_{hemi} is the experimentally observed wait time of an individual virus, N_{hemi} is the number of viruses experimentally observed to undergo lipid mixing, and N_{not} is the number of viruses that did not undergo lipid mixing. Fitting is then performed by minimizing the negative log likelihood expression across all experimentally measured pH values, written as

$$\text{NLL}(k) = - \sum_{\text{pH}} \frac{\log L}{N_{\text{tot}}} \quad (5)$$

where N_{tot} is the total number of viruses analyzed at a particular pH value.

■ ASSOCIATED CONTENT

📄 Supporting Information

The Supporting Information is available free of charge on the ACS Publications website at DOI: [10.1021/acscentsci.8b00494](https://doi.org/10.1021/acscentsci.8b00494).

Additional experimental methods, DNA sequences, PCR primers, additional microscopy information, detailed implementation of kinetic models, additional validation of viral labeling and DNA insertion, and additional kinetic models (PDF)

■ AUTHOR INFORMATION

Corresponding Authors

*(S.G.B.) E-mail: sboxer@stanford.edu. Address: 380 Roth Way, Stanford CA 94305-5012. Phone: 650-723-4442.

*(P.M.K.) E-mail: kasson@virginia.edu.

ORCID

Robert J. Rawle: [0000-0003-4958-4919](https://orcid.org/0000-0003-4958-4919)

Elizabeth R. Webster: [0000-0003-2764-1118](https://orcid.org/0000-0003-2764-1118)

Peter M. Kasson: [0000-0002-3111-8103](https://orcid.org/0000-0002-3111-8103)

Steven G. Boxer: [0000-0001-9167-4286](https://orcid.org/0000-0001-9167-4286)

Author Contributions

#R.J.R. and E.R.W. made an equal contribution.

Author Contributions

E.R.W. and R.J.R. designed experiments, performed experiments, analyzed data, and wrote the paper. R.J.R. and P.M.K. wrote Matlab and Python code used in the modeling and analysis. M.J. and P.M.K. grew and harvested the virus. P.M.K. and S.G.B. designed experiments, analyzed data, and wrote the paper.

Notes

The authors declare no competing financial interest.

■ ACKNOWLEDGMENTS

This work was supported by a University of Virginia Research Development Award and a Wallenberg Academy Fellowship to P.M.K. and National Institutes of Health Grant R35 GM118044 to S.G.B. E.R.W. was supported by an NSF predoctoral fellowship and from the Stanford ChEM-H Chemistry/Biology Interface Predoctoral Training Program. The authors thank Isabel Goronzy (Stanford) for designing and performing the RT-qPCR measurements and Stephen Harrison and Luke Chao for helpful discussions on kinetic modeling.

■ REFERENCES

- (1) Larocca, R. A.; Abbink, P.; Peron, J. P. S.; Zanutto, P. M. de A.; Lampietro, M. J.; Badamchi-Zadeh, A.; Boyd, M.; Ng'ang'a, D.; Kirilova, M.; Nityanandam, R.; et al. Vaccine protection against zika virus from Brazil. *Nature* **2016**, *536*, 474–478.
- (2) Sapparapu, G.; Fernandez, E.; Kose, N.; Cao, B.; Fox, J. M.; Bombardi, R. G.; Zhao, H.; Nelson, C. A.; Bryan, A. L.; Barnes, T.; et al. Neutralizing human antibodies prevent zika virus replication and fetal disease in mice. *Nature* **2016**, *540*, 443–447.
- (3) Haddow, A. D.; Schuh, A. J.; Yasuda, C. Y.; Kasper, M. R.; Heang, V.; Huy, R.; Guzman, H.; Tesh, R. B.; Weaver, S. C. Genetic characterization of zika virus strains: geographic expansion of the Asian lineage. *PLoS Neglected Trop. Dis.* **2012**, *6*, No. e1477.
- (4) Shan, C.; Muruato, A. E.; Jagger, B. W.; Richner, J.; Nunes, B. T. D.; Medeiros, D. B. A.; Xie, X.; Nunes, J. G. C.; Morabito, K. M.; Kong, W.-P.; et al. A single-dose live-attenuated vaccine prevents zika virus pregnancy transmission and testis damage. *Nat. Commun.* **2017**, *8*, 676.
- (5) Nour, A. M.; Li, Y.; Wolenski, J.; Modis, Y. Viral membrane fusion and nucleocapsid delivery into the cytoplasm are distinct events in some flaviviruses. *PLoS Pathog.* **2013**, *9*, e1003585.
- (6) Espósito, D. L. A.; Nguyen, J. B.; DeWitt, D. C.; Rhoades, E.; Modis, Y. Physico-chemical requirements and kinetics of membrane fusion of flavivirus-like particles. *J. Gen. Virol.* **2015**, *96*, 1702–1711.
- (7) Gollins, S. W.; Porterfield, J. S. PH-dependent fusion between the flavivirus west nile and liposomal model membranes. *J. Gen. Virol.* **1986**, *67*, 157–166.
- (8) Modis, Y.; Ogata, S.; Clements, D.; Harrison, S. C. Structure of the dengue virus envelope protein after membrane fusion. *Nature* **2004**, *427*, 313–319.
- (9) Mukherjee, S.; Sirohi, D.; Dowd, K.; Chen, Z.; Diamond, M.; Kuhn, R.; Pierson, T. C. Enhancing dengue virus maturation using a stable furin over-expressing cell line. *Virology* **2016**, *497*, 33–40.
- (10) Kostyuchenko, V. A.; Zhang, Q.; Tan, J. L.; Ng, T.-S.; Lok, S.-M. Immature and mature dengue serotype 1 virus structures provide insight into the maturation process. *J. Virol.* **2013**, *87*, 7700–7707.
- (11) Dowd, K. a.; Mukherjee, S.; Kuhn, R. J.; Pierson, T. C. Combined effects of the structural heterogeneity and dynamics of flaviviruses on antibody recognition. *J. Virol.* **2014**, *88*, 11726–11737.
- (12) Zaitseva, E.; Yang, S.-T.; Melikov, K.; Pourmal, S.; Chernomordik, L. V. Dengue virus ensures its fusion in late endosomes using compartment-specific lipids. *PLoS Pathog.* **2010**, *6*, e1001131.
- (13) Bressanelli, S.; Stiasny, K.; Allison, S. L.; Stura, E. A.; Duquerroy, S.; Lescar, J.; Heinz, F. X.; Rey, A. Structure of a flavivirus envelope glycoprotein in its low-pH-induced membrane fusion conformation. *EMBO J.* **2004**, *23*, 728–738.
- (14) Kanai, R.; Kar, K.; Anthony, K.; Gould, L. H.; Ledizet, M.; Fikrig, E.; Marasco, W. A.; Koski, R. A.; Modis, Y. Crystal structure of west nile virus envelope glycoprotein reveals viral surface epitopes. *J. Virol.* **2006**, *80*, 11000–11008.

- (15) Kuhn, R. J.; Zhang, W.; Rossmann, M. G.; Pletnev, S. V.; Corver, J.; Lenches, E.; Jones, C. T.; Mukhopadhyay, S.; Chipman, P. R.; Strauss, E. G.; et al. Structure of dengue virus: implications for flavivirus organization, maturation, and fusion. *Cell* **2002**, *108*, 717–725.
- (16) Richard, A. S.; Shim, B.-S.; Kwon, Y.-C.; Zhang, R.; Otsuka, Y.; Schmitt, K.; Berri, F.; Diamond, M. S.; Choe, H. AXL-dependent infection of human fetal endothelial cells distinguishes zika virus from other pathogenic flaviviruses. *Proc. Natl. Acad. Sci. U. S. A.* **2017**, *114*, 2024–2029.
- (17) Nowakowski, T. J.; Pollen, A. A.; Di Lullo, E.; Sandoval-Espinosa, C.; Bershteyn, M.; Kriegstein, A. R.; Wu, X.; Lemke, G.; Lu, Q.; Picone, O.; et al. Expression analysis highlights axl as a candidate zika virus entry receptor in neural stem cells. *Cell Stem Cell* **2016**, *18*, 591–596.
- (18) Hamel, R.; Dejarnac, O.; Wichit, S.; Ekchariyawat, P.; Neyret, A.; Luplertlop, N.; Perera-Lecoin, M.; Surasombatpattana, P.; Talignani, L.; Thomas, F.; et al. Biology of zika virus infection in human skin cells. *J. Virol.* **2015**, *89*, 8880–8896.
- (19) Harrison, S. C. Immunogenic cross-talk between dengue and zika viruses. *Nat. Immunol.* **2016**, *17*, 1010–1012.
- (20) Moller-Tank, S.; Kondratowicz, A. S.; Davey, R. A.; Rennert, P. D.; Maury, W. Role of the phosphatidylserine receptor tim-1 in enveloped-virus entry. *J. Virol.* **2013**, *87*, 8327–8341.
- (21) Melikyan, G. B.; Barnard, R. J. O.; Abrahamyan, L. G.; Mothes, W.; Young, J. A. T. Imaging individual retroviral fusion events: from hemifusion to pore formation and growth. *Proc. Natl. Acad. Sci. U. S. A.* **2005**, *102*, 8728–8733.
- (22) Matos, P. M.; Marin, M.; Ahn, B.; Lam, W.; Santos, N. C.; Melikyan, G. B. Anionic lipids are required for vesicular stomatitis virus g protein-mediated single particle fusion with supported lipid bilayers. *J. Biol. Chem.* **2013**, *288*, 12416–12425.
- (23) Zaitseva, E.; Zaitsev, E.; Melikov, K.; Arakelyan, A.; Marin, M.; Villasmil, R.; Margolis, L. B.; Melikyan, G. B.; Chernomordik, L. V. Fusion stage of hiv-1 entry depends on virus-induced cell surface exposure of phosphatidylserine. *Cell Host Microbe* **2017**, *22*, 99–110.
- (24) Lakadamyali, M.; Rust, M. J.; Babcock, H. P.; Zhuang, X. Visualizing infection of individual influenza viruses. *Proc. Natl. Acad. Sci. U. S. A.* **2003**, *100*, 9280–9285.
- (25) Van Der Schaar, H. M.; Rust, M. J.; Chen, C.; Van Der Ende-Metselaar, H.; Wilschut, J.; Zhuang, X.; Smit, J. M. Dissecting the cell entry pathway of dengue virus by single-particle tracking in living cells. *PLoS Pathog.* **2008**, *4*, No. e1000244.
- (26) Chao, L. H.; Klein, D. E.; Schmidt, A. G.; Peña, J. M.; Harrison, S. C. Sequential conformational rearrangements in flavivirus membrane fusion. *eLife* **2014**, *3*, No. e04389, DOI: 10.7554/eLife.04389.
- (27) Floyd, D. L.; Ragains, J. R.; Skehel, J. J.; Harrison, S. C.; van Oijen, A. M. Single-particle kinetics of influenza virus membrane fusion. *Proc. Natl. Acad. Sci. U. S. A.* **2008**, *105*, 15382–15387.
- (28) Wessels, L.; Elting, M. W.; Scimeca, D.; Weninger, K. Rapid membrane fusion of individual virus particles with supported lipid bilayers. *Biophys. J.* **2007**, *93*, 526–538.
- (29) Costello, D. A.; Lee, D. W.; Drewes, J.; Vasquez, K. A.; Kisler, K.; Wiesner, U.; Pollack, L.; Whittaker, G. R.; Daniel, S. Influenza virus-membrane fusion triggered by proton uncaging for single particle studies of fusion kinetics. *Anal. Chem.* **2012**, *84*, 8480–8489.
- (30) Rawle, R. J.; Boxer, S. G.; Kasson, P. M. Disentangling viral membrane fusion from receptor binding using synthetic dna-lipid conjugates. *Biophys. J.* **2016**, *111*, 123–131.
- (31) Harrison, S. C. Viral membrane fusion. *Virology* **2015**, *479*–480, 498–507.
- (32) Hsu, H.-L.; Millet, J. K.; Costello, D. A.; Whittaker, G. R.; Daniel, S.; Sandman, P. M.; Lanard, J.; Taubenberger, J. K.; Morens, D. M.; Dawood, F. S.; et al. Viral fusion efficacy of specific h3n2 influenza virus reassortant combinations at single-particle level. *Sci. Rep.* **2016**, *6*, 35537.
- (33) Kim, I. S.; Jenni, S.; Stanifer, M. L.; Roth, E.; Whelan, S. P. J.; Van Oijen, A. M.; Harrison, S. C. Mechanism of membrane fusion induced by vesicular stomatitis virus G protein. *Proc. Natl. Acad. Sci. U. S. A.* **2017**, *114*, E28–E36.
- (34) Chan, Y.-H. M.; Lenz, P.; Boxer, S. G. Kinetics of dna-mediated docking reactions between vesicles tethered to supported lipid bilayers. *Proc. Natl. Acad. Sci. U. S. A.* **2007**, *104*, 18913–18918.
- (35) Kyoung, M.; Zhang, Y.; Diao, J.; Chu, S.; Brunger, A. T. Studying calcium-triggered vesicle fusion in a single vesicle-vesicle content and lipid-mixing system. *Nat. Protoc.* **2012**, *8*, 1–16.
- (36) Massey, F. J. The kolmogorov-smirnov test for goodness of fit. *J. Am. Stat. Assoc.* **1951**, *46*, 68–78.
- (37) Chu, J. J. H.; Ng, M. L. Infectious entry of west nile virus occurs through a clathrin-mediated endocytic pathway. *J. Virol.* **2004**, *78*, 10543–10555.
- (38) Zheng, A.; Yuan, F.; Kleinfelter, L. M.; Kielian, M. A toggle switch controls the low ph-triggered rearrangement and maturation of the dengue virus envelope proteins. *Nat. Commun.* **2014**, *5*, 3877.
- (39) Zhang, X.; Sheng, J.; Austin, S. K.; Hoornweg, T. E.; Smit, J. M.; Kuhn, R. J.; Diamond, M. S.; Rossmann, M. G. Structure of acidic ph dengue virus showing the fusogenic glycoprotein trimers. *J. Virol.* **2015**, *89*, 743–750.
- (40) Fritz, R.; Stiasny, K.; Heinz, F. Identification of specific histidine residues as ph sensors in flavivirus membrane fusion. *J. Cell Biol.* **2008**, *183*, 353–361.
- (41) White, J. M.; Delos, S. E.; Brecher, M.; Schornberg, K. Structures and mechanisms of viral membrane fusion proteins: multiple variations on a common theme. *Crit. Rev. Biochem. Mol. Biol.* **2008**, *43*, 189–219.
- (42) Yang, S.-T.; Zaitseva, E.; Chernomordik, L. V.; Melikov, K. Cell-penetrating peptide induces leaky fusion of liposomes containing late endosome-specific anionic lipid. *Biophys. J.* **2010**, *99*, 2525–2533.
- (43) Stiasny, K.; Fritz, R.; Pangerl, K.; Heinz, F. X. Molecular mechanisms of flavivirus membrane fusion. *Amino Acids* **2011**, *41*, 1159–1163.
- (44) Persaud, M.; Martinez-Lopez, A.; Buffone, C.; Porcelli, S. A.; Diaz-Griffero, F. Infection by zika viruses requires the transmembrane protein axl, endocytosis and low ph. *Virology* **2018**, *518*, 301–312.
- (45) Ivanovic, T.; Choi, J. L.; Whelan, S. P.; Van Oijen, A. M.; Harrison, S. C. Influenza-virus membrane fusion by cooperative fold-back of stochastically induced hemagglutinin intermediates. *eLife* **2013**, *2*, DOI: 10.7554/eLife.00333.
- (46) Sirohi, D.; Kuhn, R. J. Zika virus structure, maturation, and receptors. *J. Infect. Dis.* **2017**, *216*, S935–S944.
- (47) Kuhn, R. J.; Dowd, K. A.; Beth Post, C.; Pierson, T. C. Shake, rattle, and roll: impact of the dynamics of flavivirus particles on their interactions with the host. *Virology* **2015**, *479*–480, 508–517.
- (48) White, J. M.; Whittaker, G. R. Fusion of enveloped viruses in endosomes. *Traffic* **2016**, *17*, 593–614.
- (49) Zhang, S.; Kostyuchenko, V. A.; Ng, T.-S.; Lim, X.-N.; Ooi, J. S. G.; Lambert, S.; Tan, T. Y.; Widman, D. G.; Shi, J.; Baric, R. S. Neutralization mechanism of a highly potent antibody against zika virus. *Nat. Commun.* **2016**, *7*, 13679.
- (50) Klein, D. E.; Choi, J. L.; Harrison, S. C. Structure of a dengue virus envelope protein late-stage fusion intermediate. *J. Virol.* **2013**, *87*, 2287–2293.
- (51) Hughes, L. D. Model membrane architectures for the study of membrane proteins. Doctoral Dissertation, Stanford University, **2013**. <https://purl.stanford.edu/xr495nv6897>. Accessed July 20, 2018.
- (52) Medina, F.; Medina, J. F.; Colón, C.; Vergne, E.; Santiago, G. A.; Muñoz-Jordán, J. L. Dengue virus: isolation, propagation, quantification, and storage. *Curr. Protoc. Microbiol.* **2012**, *27*, 15D.2.1–15D.2.24.

SI Appendix: “pH Dependence of Zika Membrane Fusion Kinetics Reveals an Off-Pathway State”

Authors: Robert J. Rawle^{a,1}, Elizabeth R. Webster^{b,1}, Marta Jelen^a, Peter M. Kasson^{a,c,2}, Steven G. Boxer^{*b,2}

Author affiliations:

a. Departments of Molecular Physiology and Biological Physics and of Biomedical Engineering, University of Virginia, Charlottesville VA 22908.

b. Department of Chemistry, Stanford University, Stanford CA 94305.

c. Science for Life Laboratory, Department of Cell and Molecular Biology, Uppsala University, Uppsala SE 75124

1. equal contribution

2. To whom correspondence should be addressed: sboxer@stanford.edu and kasson@virginia.edu; 380 Roth Way, Stanford CA 94305-5012; 650-723-4442.

Table of Contents

S1. Supplementary Methods

S1.1 Flow cell and glass coverslip preparation

S1.2 Functionalized glass coverslips for tethered vesicles

S1.3 Vesicle preparation

S1.4 DNA-lipid mediated viral tethering to supported lipid bilayers

S1.5 Immunofluorescence assay of DNA-lipid tethered Zika virus

S1.6 DNA-lipid, alkyne-DNA, and 488-DNA-lipid preparation

Table S1. DNA-lipid used

S1.7 Western Blot

S1.8 Viral RNA quantitation

Table S2. PCR primers used

S1.9 Additional Microscopy Details

S1.10 Image Analysis

S1.11 Simple Kinetic Modeling

S1.12 Cellular Automaton Simulation Model

S1.13 Data Fitting with the Cellular Automaton Model

S2. Supplementary Results

Figure S1. Western Blot of Zika virus following purification.

Figure S2. Immunofluorescence assay of Zika virus tethered to a supported bilayer via DNA-lipids

Figure S3. Distribution of DNA lipid tethers incorporated into Zika virions.

Figure S4. Zika virus binds specially to bilayers through complementary DNA lipids.

Figure S5. Increasing dye concentration in viral labeling does not alter the lipid mixing efficiency.

S2.1 Quantification of Zika virus lipid mixing events at pH 7.4 and inactivation

Figure S6. Inactivated Zika virus exhibits no hemifusion.

Figure S7: A linear model cannot simultaneously fit the normalized CDF and the efficiency of the experimental data.

Figure S8: Addition of a non-rate limiting step to the linear model does not substantially alter the fit.

Figure S9: Addition of an initial step that is not rate limiting to the off-pathway model does not substantially alter the fit.

Figure S10. Allowing two parameter variance does not improve the fit of the Linear model with the experimental data.

Figure S11: Estimate of optimal pH at which the off-pathway state is 50% populated.

Figure S12: Comparison of Simple Kinetic Models for the Hemifusion Kinetics of Zika Virus.

Figure S13: Background Correction of Hemifusion Kinetics.

S3. Cellular Automaton Model

Figure S14. Implementation of the cellular automaton using the linear model shown in Equation S1 is unable to fit the experimental data.

Figure S15. The addition of an off-pathway state to the cellular automaton models is necessary to describe the experimental trends in both the efficiencies and rates of single virus lipid mixing data.

S3.1 Effect of delay time between virus binding and pH drop on experimental hemifusion efficiencies.....

Figure S16. Doubling the delay time between virus binding and buffer exchange to low pH did not significantly affect the relative hemifusion efficiency.

S4. References

S1. Supplementary Methods

S1.1 Flow cell and glass coverslip preparation

Glass coverslips were cleaned and then plasma bonded to polydimethylsiloxane (PDMS) flow cells as previously described in detail ¹. Briefly, glass coverslips (24 x 40 mm, No 1.5, VWR International, Randor, PA) were cleaned with a 1:7 solution of 7x detergent in DI water heated to clarity for 25 min, rinsed extensively with DI water, then kiln baked for 4 hrs at 400°C. PDMS flow cells (channel dimensions = 2.5 mm x 13 mm x 70 µm) were prepared by tape based soft lithography. The PDMS flow cell and clean coverslip were plasma cleaned for 1 min and then bonded together.

S1.2 Functionalized Glass coverslips for tethered vesicles

Clean glass coverslips were functionalized by silanization, then azide-alkyne click chemistry was used to attach DNA oligomers to the surface as described in detail in ¹. In brief, clean coverslips were silanized using vapor deposition of 11- Azidoundecyltrimethoxysilane to yield azide-functionalized glass. PDMS flow cells were glued with epoxy to the functionalized coverslips and DNA alkyne Sequence B (see Table S1) was covalently bound to the surface in the presence of 20 mM sodium ascorbate, 0.43 mM copper (II) sulfate, and 0.86 mM (triethyl 2,2',2''-(4,4',4''-nitrioltris(methylene)tris(1H-1,2,3-triazole-4,1-diyl))triacetate (TTMA) ligand for at least one hour then rinsed. To passivate any unreacted azide, ethynyl phosphonic acid was incubated in the flow cell with 20 mM sodium ascorbate, 0.43 mM copper (II) sulfate, and 0.86 mM TTMA ligand for at least an hour then rinsed with DI water. The DNA-functionalized flow cell displaying Sequence B could be used directly, or stored overnight at 4°C. To tether vesicles, the flow cells were rinsed with RB then 6 µL of .56 mM of 100 nm vesicles suspension displaying 0.01 mol% DNA-lipids of Sequence B' in RB (reaction buffer; ~500 µM suspended lipids) was added to the flow cell channel and incubated at 23 C for at least 60 min then rinsed with RB.

S1.3 Vesicle preparation

A lipid mixture of 69.9% POPC, 20% DOPE, 10% Chol, 0.01% Oregon Green- DHPE was prepared in chloroform, then dried down to a film under nitrogen gas, and then under vacuum for several hours to remove any residual solvent. Then, the lipid film was re-suspended by vortexing in RB and extruded through a track-etched polycarbonate membrane (100 nm pore size, Avanti Polar Lipids) using a mini extruder (Avanti Polar Lipids) to yield large unilamellar vesicles. DNA-lipids were then added at the indicated mole percent, and incubated overnight at 4°C. This procedure incorporates the DNA-lipids into the outer leaflet of the vesicles. Vesicle suspensions were stored at 4°C and used within 5 days. To calibrate the time of pH drop, a lipid mix of 68% POPC, 20% DOPE, 10% Chol, 2% Oregon Green- DHPE was used.

S1.4 DNA-lipid mediated viral tethering to supported lipid bilayers

6 µL of vesicles (~500 µM total lipids) containing 0.05 mol% DNA-lipids (Sequence A') were added to the flow cell channel and incubated at room temperature for 20 min to form a supported lipid bilayer. The bilayer was then rinsed with 1 mL of DI water followed by 2 mL of RB. Texas-Red labeled Zika virions with incorporated DNA-lipids (Sequence A) were then tethered to the lipid bilayer. The cell was washed extensively with RB to remove any unbound virions. Fluorescent micrographs of at least 10 different fields of view were collected to visualize the bound virions, and the number of bound virions was quantified by image analysis. Interestingly, the DNA-lipid mediated binding occurred qualitatively faster for Zika virus as compared with the binding of influenza in previous work ¹. We speculate that the difference in binding may be related to the difference in size between the envelope protein (Zika) and hemagglutinin (influenza).

S1.5 Immunofluorescence assay of DNA-lipid tethered Zika virus

Zika virions (displaying DNA-lipid Sequence A) were bound to a supported lipid bilayer containing 0.05 mol% DNA-lipids (Sequence A') inside a flow cell, as described above. Following the final wash, the cell was incubated with a 1:1000 dilution of 4G2 anti-flavivirus primary antibody for 2 hours at 23 °C, then washed with RB. The flow cell was then infused with 1:100 dilution of Alexa 488-goat anti-mouse secondary antibody, incubated for at least 20 minutes, washed and then imaged by fluorescence microscopy. Texas Red and Alexa 488 images were collected sequentially. Some virus particles remained mobile by Brownian diffusion on the bilayer surface leading to negligible error in the colocalization data.

S1.6 DNA-lipid, alkyne-DNA, and 488-DNA-lipid preparation

DNA-lipids used to tether virions to target vesicles were synthesized as previously described in detail ^{1,2}. Briefly, DNA oligomers were synthesized by the Protein and Nucleic Acid Facility at Stanford University, covalently coupled on resin to the lipid tail by phosphoramidite chemistry, and HPLC purified. Alkyne-DNA used to functionalize glass coverslips was synthesized by the Protein and Nucleic Acid Facility at Stanford University, then purified by HPLC or ethanol precipitation upon receipt. Alexa 488-labeled DNA-lipids, used to determine the number of DNA-lipids per virion, were prepared by NHS coupling of Alexa 488 succinimidyl ester to the DNA lipid via a 3' amine as previously described ³. We tested several different DNA-lipid sequences to tether Zika virus to target membranes. We observed that the sequence used could significantly affect the density of viral particles bound. Sequences A and A' were found to be optimal in facilitating binding. When the fully overlapping sequences of B and B' were used in the viral membrane and tethered vesicles, binding was severely depressed. We hypothesize that there may have been interaction between the DNA sequence with the virus which prevented the full hybridization.

Table S1. DNA-lipids, DNA-alkyne, and dye labeled DNA-lipid sequences used

Name	DNA Sequence(5'-3')	Complementary Sequence	Location
A	Lipid - AAA AAA AAA AAA AAA AAA AAA AAA	A'	Viral envelope
A'	Lipid - TTT TTT TTT TTT TTT TTT TTT TTT	A	Vesicle
B	Alkyne - TCC TGT GTG AAA TTG TTA TCC GCA	B	Glass slide
B'	Lipid - TGC GGA TAA CAA TTT CAC ACA GGA	B'	Vesicle
X	Lipid - AAA AAA AAA AAA AAA AAA AAA AAA -Alexa 488	Not used	Viral envelope

S1.7 Immunoblots

Serial dilutions of resuspended viral pellet and supernatant were diluted in 1x TRIS glycine-SDS buffer and 1x loading buffer, heated at 90 °C for 5 min then run on a TRIS glycine-SDS 4-20% gel under non-reducing conditions. The proteins were transferred to a nitrocellulose membrane which was blocked at 4 °C overnight. A 1:5000 dilution of 4G2 anti-flavivirus primary was added blocking buffer and incubated at 25°C for 1 hr then washed. For visualization, a 1:10,000 dilution of IRDye® 680RD Goat anti-Mouse IgG in blocking buffer was incubated at 25 °C for one hour, then washed and imaged on a LiCor Odyssey. Blocking buffer = 5% w/v milk powder, 0.05% Tween in TBS buffer.

S1.8 Viral RNA quantitation

Total RNA content of Zika samples was quantified from extracted vRNA by RT-qPCR and using a standard curve correlating threshold cycle number to RNA concentration. First, viral RNA was extracted using the Zymo Research ZR Viral RNA Kit, according to manufacturer's recommendations and analyzed by RT-qPCR. Total RNA content of each sample was determined using the Power SYBR® Green RNA-to-CT™ 1-Step Kit (Thermo Fisher Scientific). Primers were designed to amplify a 100-base-pair region of the Zika virus strain ZIKV/*Aedes africanus*/SEN/DakAr41524/1984 and were synthesized by the Protein and Nucleic Acid Facility at Stanford.

Table S2. Forward and reverse primer sequences for PCR.

	Designation Sequence (5'→3')
Forward Primer	CAGCTGGCATCATGAAGAATC
Reverse Primer	CACTTGTCCCATCTTCTTCTCC

RNA of the sample was extracted as described above and then amplified using the QIAGEN OneStep RT-PCR kit (QIAGEN). Primers were identical to those for rRT-qPCR experiments. Amplified DNA was isolated using GENEJET PCR Purification Kit (Thermo Fisher Scientific) and quantified via absorbance at 260nm using an estimated extinction coefficient of 806,000 L mol⁻¹ cm⁻¹. Different viral batches yielded different concentrations of viral RNA, as expected, but a representative concentration was 2.4 x 10⁻¹⁴ vRNA U/mL following labeling and purification. A mock-labeled viral sample from the same batch yielded 1.5 x 10⁻¹³ vRNA U/mL.

S1.9 Additional Microscopy Details

Texas Red images utilized a Texas Red filter cube (ex = 562/40 nm, bs = 593 nm, em = 624/40 nm), and additional excitation (ex = 560/55 nm) and emission (em = 645/75 nm) filters. Oregon Green images utilized a NBD filter cube (ex = 475/35 nm, bs = 509 nm, em = 528/38 nm), and additional excitation (ex = 460/50 nm) and emission (em = 535/50 nm) filters. All images and video micrographs were captured at 288 ms/ frame.

S1.10 Image Analysis

Custom Matlab scripts (MathWorks, Inc.) were used to analyze the microscopy images and video micrographs as described previously¹ and are available at <https://github.com/kassonlab/micrograph-spot-analysis>.

S1.11 Simple Kinetic Modeling

The simple kinetics models in the SI were constructed as described in the main text Kinetic modeling section with the following differences. We used the unconstrained Nelder-Mead algorithm implemented in Matlab (fminsearch) to minimize the negative log likelihood function. Initial parameter values were set by grid search across the set of rate constant parameters being varied. To fit the experimental data using relative efficiency values, experimental efficiency values (π_{exp}) were normalized to the efficiency at pH 4.6, in which case $N_{not} = N_{hemi}/\pi_{exp,norm} - N_{hemi}$, and $N_{tot} = N_{not} + N_{hemi}$. This treatment assumes that the observed efficiency at pH 4.6 is the maximum efficiency of the experimental system, which is consistent with the observation that roughly doubling the length of the video stream at pH 4.6 did not substantially alter the resulting efficiency.

S1.12 Cellular Automaton Simulation Model

The cellular automaton model was re-implemented in Matlab based on the algorithm described in⁴. Matlab code for our implementation is available at <https://github.com/kassonlab>. The general outline and state definitions of the model are described in the Section S3 below, and additional changes made to implement the algorithm are as follows. For each E protein

monomer in the cellular automaton simulation, the probability of a given state transition within a simulation time step was calculated by solving the kinetic master equation using matrix exponentials. This transition probability matrix depended on the geometrical state of the E monomer (e.g. trimerization was only allowed if at least two nearby neighbors were extended, etc.). The cooperativity factor (CF) was implemented as $k_{\text{ext}} = \text{CF} \cdot k_{\text{act}} \cdot [\text{H}^+]$ if a given monomer's dimer partner was already extended.

The time step of each simulation was set such that the maximum transition probability between any two adjacent states was 0.1. The minimum allowed time step was 1 ms. To determine the starting state of the simulation, viruses were allowed to equilibrate between State 1 and 2 at pH 7.4, as discussed in Section S3. The pH was then dropped and the simulation was run until $t = 340$ s, corresponding to our experimentally observed time window. The wait time of each virus which underwent lipid mixing during the simulation was recorded.

S1.13 Data Fitting with the Cellular Automaton Model

Data fitting was performed using the maximum likelihood formulation described in the Kinetic Modeling methods section with the following differences. f_{hemi} (Eqn. 3, main text) was estimated from the cellular automaton wait times using bounded kernel density estimation with boundary reflection⁵. A direct search algorithm implemented in Matlab (using the Matlab `patternsearch` routine) was used to minimize the Negative Log Likelihood (NLL) (Eqns. 4 and 5, main text). For each pH value at each iteration of the minimization algorithm, groups of 1200 viruses were simulated until 1000 viruses underwent lipid mixing or until 12,000 viruses had been simulated. For all data fitting, the CF was set at 1. For the best fit solutions of the linear model, CF values in the range of 1-10 did not substantially alter the ability of the model to fit the data. The best fit values reported for all models converged to within the stochastic estimation error. Note that the reported values for k_{tri} are for each monomer, which are sampled independently to initiate trimer formation. Similarly, the values for k_{Hfuse} are for each trimer, which are sampled independently to initiate hemifusion.

S2. Supplementary Results

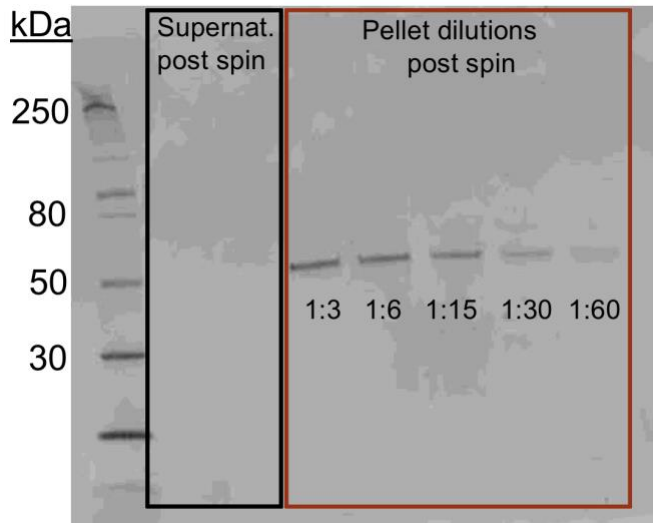


Figure S1. Western Blot of Zika virus following ultra-centrifugation through a 20% sucrose cushion. SDS-PAGE immunoblots were performed on samples taken from the supernatant and the resuspended pellet following centrifugation using a 4G2 anti-flavivirus E protein primary antibody and a goat anti-mouse IR 680 secondary antibody. The single band at ~50kDa is consistent with a dimer of E protein. Dilutions of the pellet from left to right: 1:3, 1:6, 1:15, 1:30, 1:60.

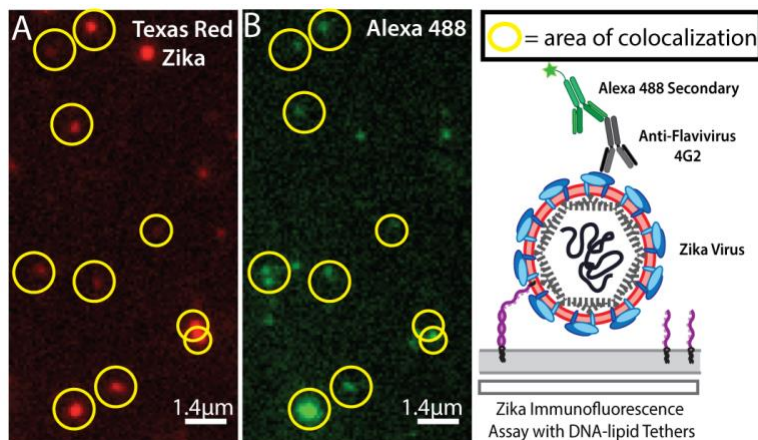


Figure S2. Immunofluorescence assay of Zika virus tethered to a supported bilayer via DNA-lipids. To further ensure that viral particles were properly labeled, an immunofluorescence assay was performed on Texas-Red-labeled viral particles tethered via DNA-lipid hybridization (Sequence A-A' in Table S1) to a glass supported bilayer. Anti-flavivirus E protein 4G2 primary was used at 1:1000 dilution followed by a goat anti-mouse Alexa-488 secondary. The colocalization of putative viral particles with secondary antibody was found to be $64\% \pm 5\%$. Additionally, negligible colocalization was observed in the absence of primary antibody. Tethered particles are mobile on the bilayer, so the observed colocalization likely underestimates co-labeling. (A) Texas-red filter image (putative virions). (B) Alexa 488 filter image.

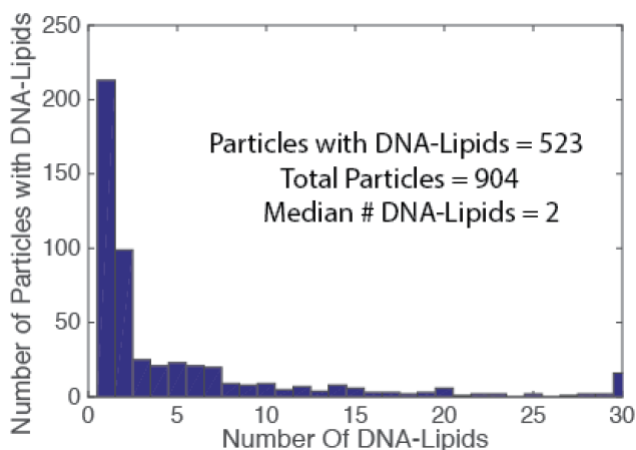


Figure S3. Quantification of the number of DNA-lipids per Zika virion.

To quantify the number of DNA-lipids per virion, we utilized an Alexa 488-labeled DNA-lipid (Sequence X, Table S1) and performed a quantitative fluorescence imaging measurement as reported previously for influenza virus^{1,2,6}. Alexa 488 DNA-lipids were incorporated into Texas-Red-labeled Zika virions, which were then non-specifically bound to a glass coverslip, rinsed thoroughly, and imaged in both the Texas Red and Alexa 488 channels. The average fluorescence intensity per Alexa 488 dye was determined by single step photo-bleaching. The number of DNA-lipids incorporated into each virion was calculated as (Alexa 488 total intensity of the virion) / (average intensity per Alexa 488 dye). We observed that the majority of virions contained fewer than 5 DNA-lipids. 58% of all virions contain at least one DNA-lipid with a median of 2 DNA lipid per virion. Total virions analyzed = 904.

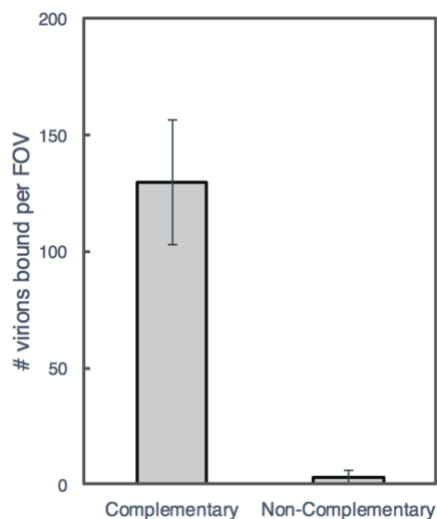


Figure S4. Zika virus binds specifically to supported bilayers through complementary DNA lipids.

DNA-lipid Sequence A was incorporated into Texas Red-labeled Zika virions. Virions were then introduced into a flow cell containing a supported lipid bilayer with either 0.01% Sequence A' (complementary) or Sequence B' (non-complementary, Table S1). The virus was incubated for roughly 10 min with each bilayer, then any unbound virus was removed by extensive rinsing of the flow cell. Bound virions were imaged by fluorescence microscopy, and the number of bound virions was quantified by image analysis. Negligible nonspecific binding was observed to supported bilayers that contained non-complementary DNA-lipids. Sequence A/A' were found to lead to the optimal number of bound virions per FOV.

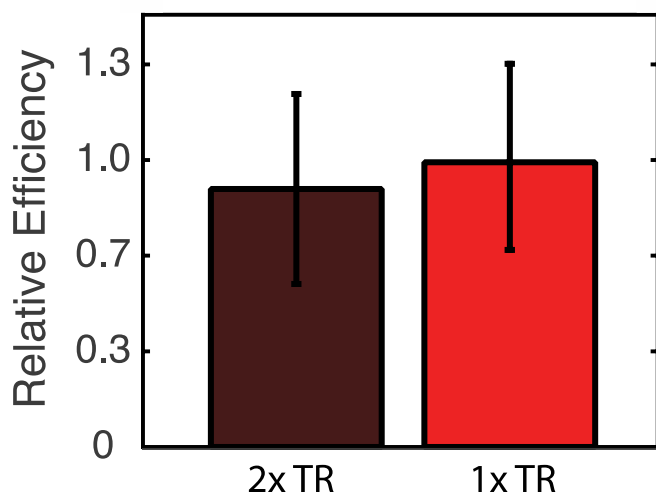


Figure S5. Increasing dye concentration in viral labeling does not alter the lipid mixing efficiency. Plotted are the relative efficiencies of single-Zika virus lipid mixing events labeled with either the 1x TR (10 μ M) or 2x TR (20 μ M). Total particles analyzed 2xTR N = 352; 1xTR N = 433.

S2.1 Quantification of Zika virus lipid mixing events at pH 7.4 and inactivation

In our lipid mixing assay (e.g. main text Figure 1), we consistently observed a low background efficiency (~3%) of lipid mixing events at pH 7.4. This low efficiency was significantly lower than at all lower pH values ($p < 5 \times 10^{-4}$). Neither lipid vesicles or influenza virus tethered to target vesicles by DNA-lipids in this orientation fuse at pH 7.4^{1,2}, indicating that the DNA-lipid tethering approach is not responsible for this neutral pH hemifusion. To determine whether these lipid mixing events were the result of competent virus, we performed our single virus lipid mixing assay on inactivated virus. The virus was inactivated by multiple freeze thaw cycles at pH 4.6, and then re-neutralized prior to tethering to target vesicles in our lipid mixing assay. Lipid mixing events of the inactivated virus at pH 7.4 and 5.4 were collected and compared to untreated virus. We observed essentially no lipid mixing within an experimental error following inactivation (Figure S6).

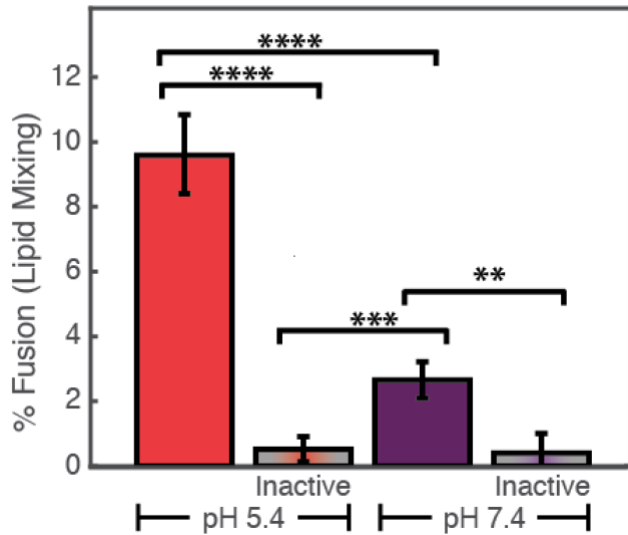


Figure S6. Inactivated Zika virus exhibits no hemifusion. Shown are the hemifusion efficiencies of single virus lipid mixing measurements performed using virus which had or had not been previously inactivated. Inactivation was performed via multiple freeze thaw cycles at pH 4.6, and then re-neutralized prior to tethering to target vesicles. Error bars were calculated from bootstrap resampling of all virions at the indicated condition. Significance was calculated using a bootstrap statistical test of the observed difference between the efficiency values, comparing to a null hypothesis that viruses from both data sets came from the same distribution **** $p \leq 0.0001$, *** $p \leq 0.001$, ** $p \leq 0.01$. $N/N_{\text{tot}} = 145/1510$ (pH 5.4), $4/800$ (pH 5.4, inactive), $61/2259$ (pH 7.4), $2/500$ (pH 7.4, inactive).

Together, this data suggests that Zika virus may undergo fusion with a target membrane at pH 7.4, when it is brought into close apposition with the target via receptor binding/DNA-lipid tethering. Such an interpretation is consistent with various lines of evidence suggesting that the E protein of closely related flaviviruses is rather dynamic and can sample conformations, even at neutral pH, which expose the hydrophobic fusion loop. For example, antibodies directed against the fusion loop of the Dengue virus E protein are able to bind successfully at pH 7.4, even when the fusion loop epitope appears to be inaccessible in the cryoEM structure⁷⁻⁹. We also observed similar results with Zika virus; the antibody we (and others) use in our immunofluorescence assay (Figure S2) is directed against the fusion loop, and binding was observed at pH 7.4. Therefore, the low level of hemifusion we observe at neutral pH may be due to the dynamic nature of the E protein: if the fusion loop is transiently exposed to a nearby target membrane in close proximity, this may be sufficient to initiate hemifusion, albeit with low efficiency. Interestingly, such a hypothesis might explain previous data from cell culture which suggested that low levels of Zika virus infection might still occur even when endocytosis was inhibited¹⁰.

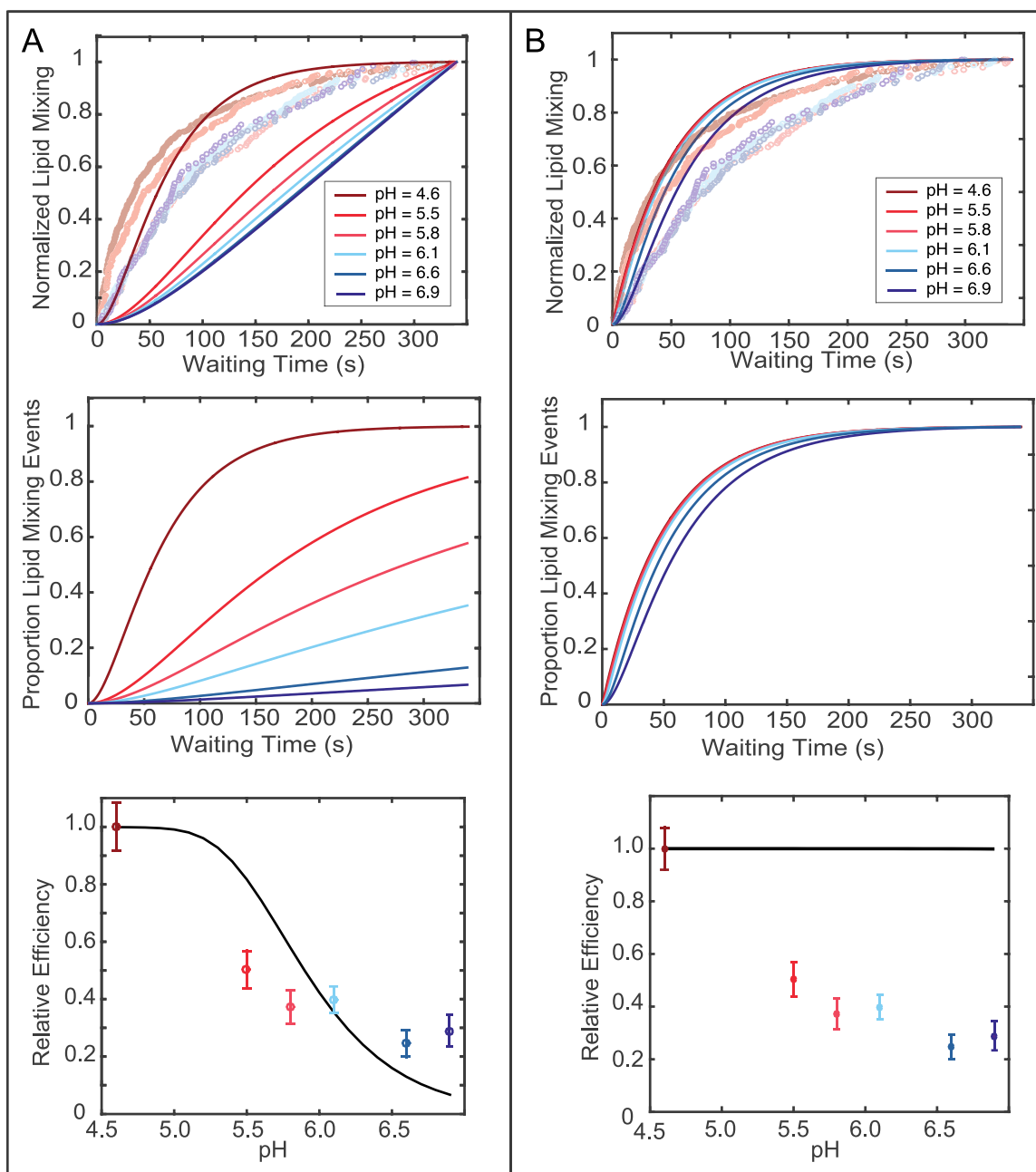


Figure S7: A linear model cannot simultaneously capture the hemifusion rates and the efficiencies of the experimental data. When k_{BA} is large, the trend in the hemifusion rates is largely captured but the efficiencies are not well described. However, when k_{BA} is lowered to more closely match the efficiencies, the lower pH values take the form of truncated gamma distributions. Including additional states in the model does not compensate for this deficiency. Linear model with low k_{BA} value, $2,000 \text{ M}^{-1} \text{ s}^{-1}$, (A) and high k_{BA} value, $50,000 \text{ M}^{-1} \text{ s}^{-1}$ (B). All other k values were kept constant. Rate constants: $k_{BA}' = k_{BA} \cdot [\text{H}^+]$; $k_{AB} = k_{BA} \cdot 10^{-8} \text{ M}$; $k_{AF} = 0.02 \text{ s}^{-1}$. Colored circles = experimental data, solid lines = model data.

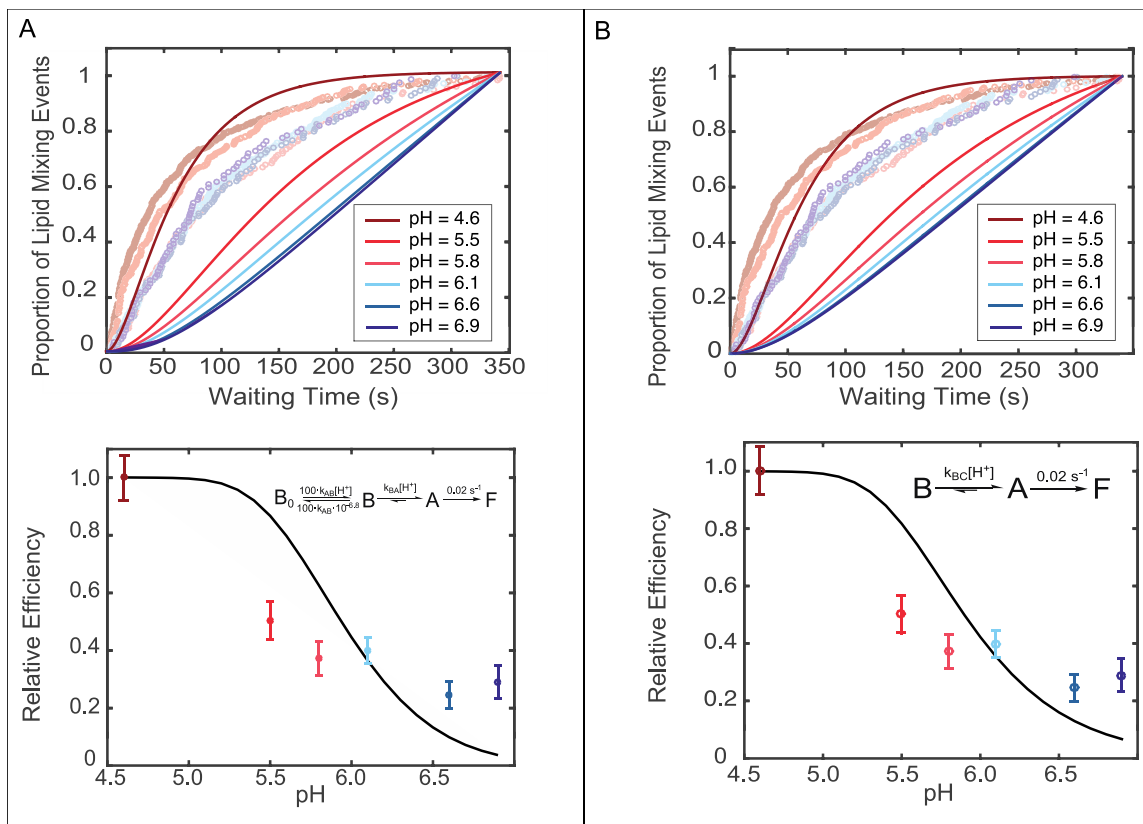


Figure S8: Addition of a step that is not rate-limiting to the linear model (Equation 1 in main text) does not substantially alter the fit. A one parameter fit of k_{BA} was performed on the four state (A) and three state model (B) to fit our experimental data. The best fit rate constants were $k_{BA} = 2,410 \text{ M}^{-1} \text{ s}^{-1}$ (A) and $k_{BA} = 1,910 \text{ M}^{-1} \text{ s}^{-1}$ (B). Other rate constants defined as: $k_{B_0B} = 100 \cdot k_{BA} \cdot [H^+]$; $k_{BB_0} = 100 \cdot k_{BA} \cdot 10^{-6.8} \text{ M}$; $k_{BA'} = k_{BA} \cdot [H^+]$; $k_{AB} = k_{BA} \cdot 10^{-8} \text{ M}$; $k_{AF} = 0.02 \text{ s}^{-1}$. Colored circles = experimental data, solid lines = model best fit.

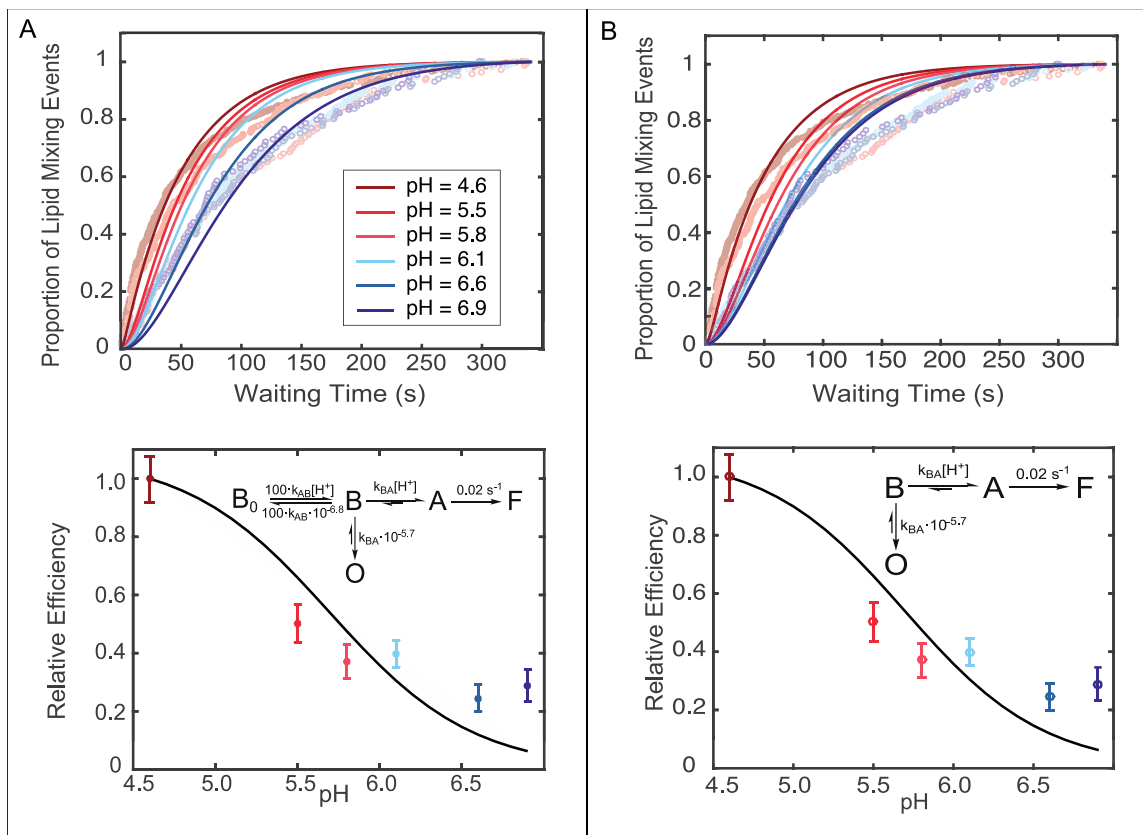


Figure S9: Addition of an initial step that is not rate limiting to the off-pathway model does not substantially alter the fit. A one parameter fit of k_{BA} was performed on the five state (A) and four state model (B) to fit our experimental data. The best fit rate constants were: $k_{BA} = 21,100 \text{ M}^{-1} \text{ s}^{-1}$ (A) and $k_{BA} = 11,100 \text{ M}^{-1} \text{ s}^{-1}$ (B). Other rate constants defined as: $k_{BOB} = 100 \cdot k_{BA} \cdot [H^+]$; $k_{BB_0} = 100 \cdot k_{BA} \cdot 10^{-6.8} \text{ M}$; $k_{BA'} = k_{BA} \cdot [H^+]$; $k_{AB} = k_{BA} \cdot 10^{-8} \text{ M}$; $k_{AO} = k_{BA} \cdot 10^{-5.7} \text{ M}$; $k_{AF} = 0.02 \text{ s}^{-1}$. Colored circles = experimental data, solid lines = model best fit.

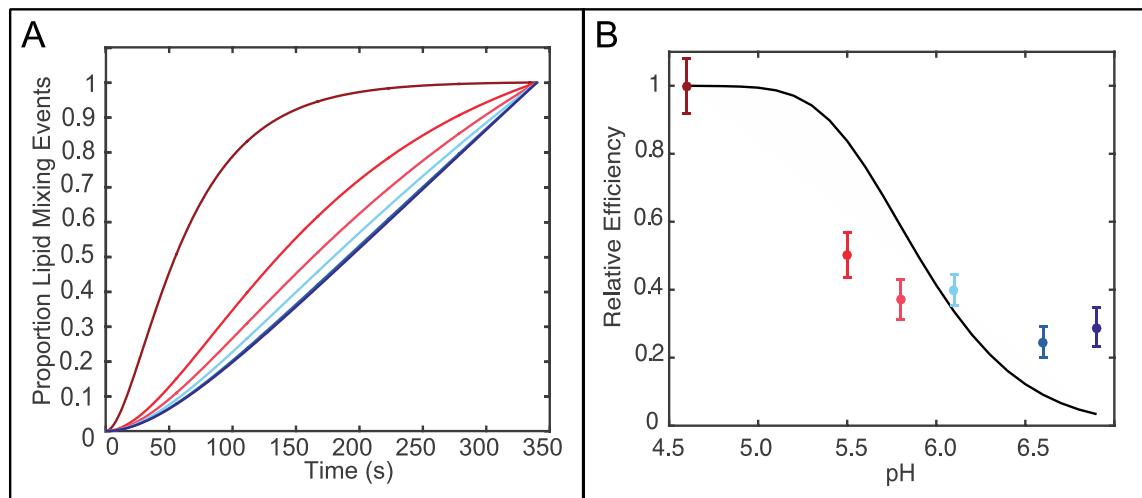


Figure S10. A two-parameter fit of a linear model to our experimental data did not qualitatively improve the best fit. A two-parameter fit of k_{BA} and k_{B0B} was performed on the four-state linear model (Eqn. A, Figure S8) to fit our experimental data. (A) Lipid mixing kinetics were all normalized to 1. (B) efficiency at pH 4.6 was normalized to 1 (B). The best fit rate constants were: $k_{B0B} = 1 \times 10^6 \text{ s}^{-1}$ and $k_{BA} = 2,150 \text{ M}^{-1} \text{ s}^{-1}$. Rate constants: $k_{B0B}' = k_{B0B} \cdot [\text{H}^+]$; $k_{BB0} = k_{B0B} \cdot 10^{-6.8} \text{ M}$; $k_{BA}' = k_{BA} \cdot [\text{H}^+]$; $k_{AB} = k_{BA} \cdot 10^{-8} \text{ M}$; $k_{AF} = 0.02 \text{ s}^{-1}$. Colored circles = data, solid lines = model best fit.

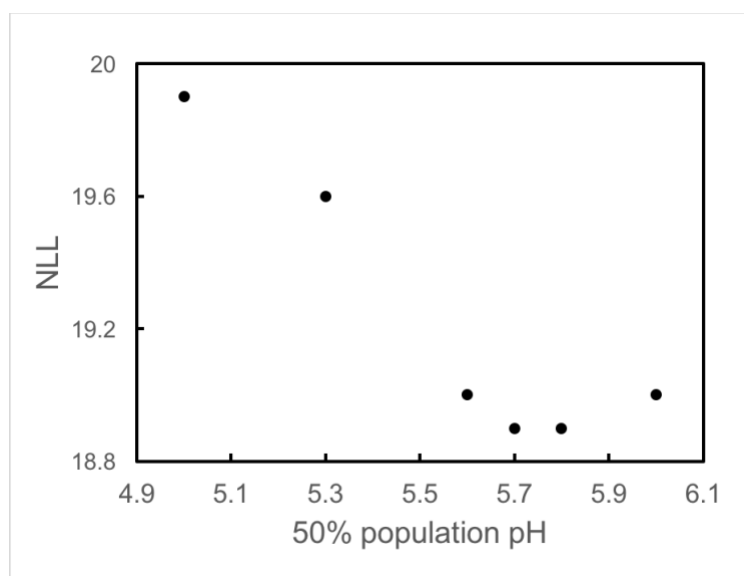


Figure S11: Estimate of optimal pH at which the off-pathway state is 50% populated. To determine the off-pathway rate constant k_{B0} , lipid-mixing efficiency data were treated as approximately linear with pH. At pH 5.7, the off-pathway state is 50% populated, leading to $k_{B0} = k_{BA} \times 10^{-5.7}$. To more fully validate this off-pathway rate constant, parameters around $k_{BA} \cdot 10^{-5.7}$ were scanned and negative log likelihood (NLL) values compared. The NLL was minimized between pH 5.7 and 5.8. Rate constants used are as follows: $k_{BA} = 11,100 \text{ M}^{-1} \text{ s}^{-1}$; $k_{BA}' = k_{BA} \cdot [\text{H}^+]$; $k_{AB} = k_{BA} \cdot 10^{-8} \text{ M}$; $k_{B0} = k_{BA} \cdot 10^{-(50\% \text{ pop pH})} \text{ M}$; $k_{AF} = 0.02 \text{ s}^{-1}$.

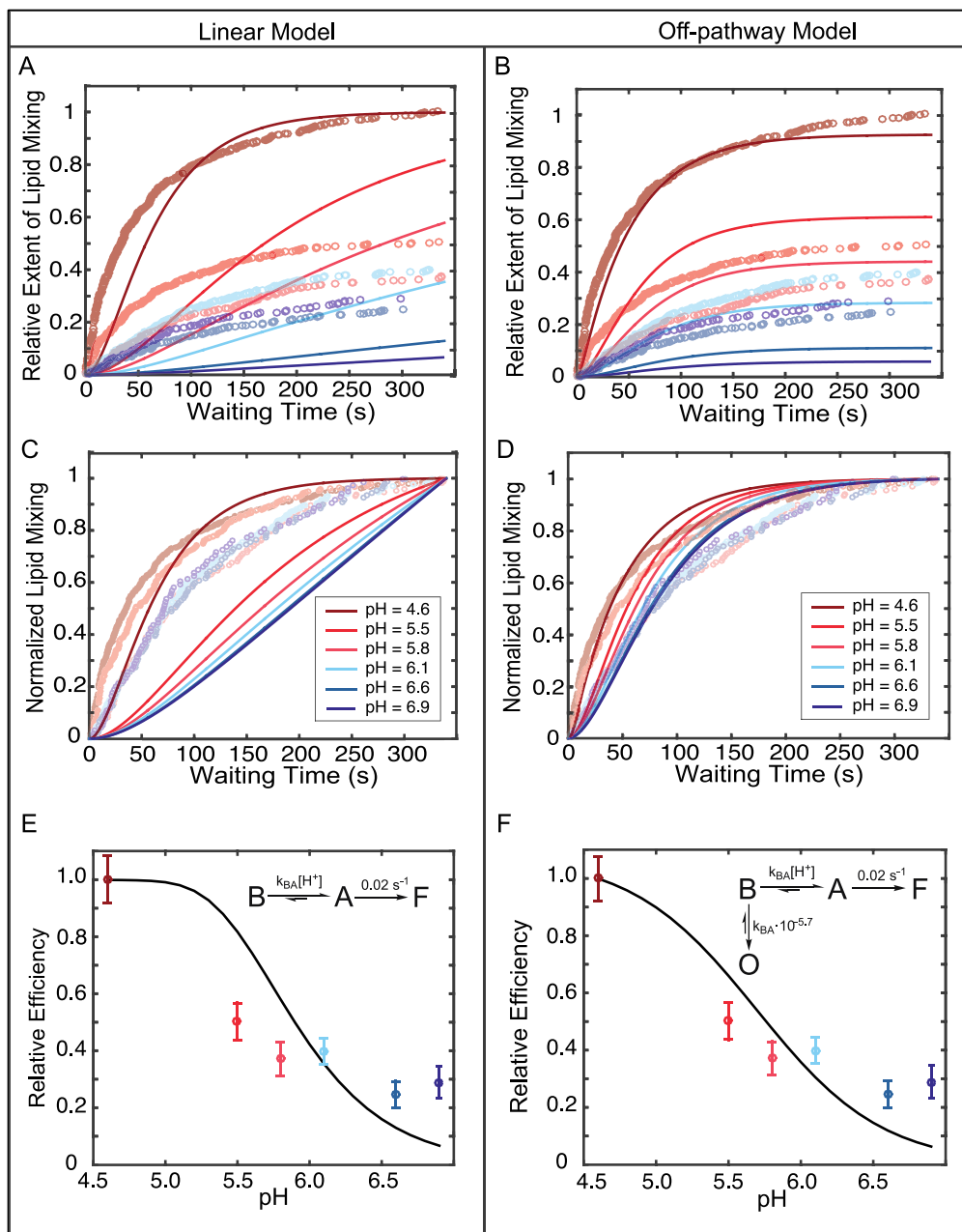


Figure S12: Comparison of simple kinetic models for the fusion kinetics of Zika Virus. Single- parameter fits of k_{BA} were performed across all pH values simultaneously to optimize the linear and off-pathway model to the experimental data. Plotted in panels A-B are lipid-mixing kinetic curves calculated from a linear model (A) and an off-pathway model (B) in solid lines, compared to observed single-virus fusion data at multiple pH values (open circles). The linear model reproduces the ordering of pH values but does not the shape of the curves. (A) The off-pathway model reproduces both the ordering of pH values and the shape of the curves but underestimates the extent of hemifusion at higher pH values. (B) Plots of lipid mixing normalized to the final value at each pH (panels C-D) further illustrate the failure of the linear model to capture the kinetics of hemifusion. Plots of lipid mixing efficiency (panels E-F). The best-fit rate constants were: $k_{BA}= 1,910\text{ M}^{-1}\text{ s}^{-1}$ (A) and $k_{BA}= 11,100\text{ M}^{-1}\text{ s}^{-1}$ (B). Other rate constants defined as: $k_{BA}' = k_{BA} \cdot [H^+]$; $k_{AB} = k_{BA} \cdot 10^{-8}\text{ M}$; $k_{BO} = k_{BA} \cdot 10^{-5.7}\text{ M}$; $k_{AF} = 0.02\text{ s}^{-1}$. Colored circles = experimental data, solid lines = model best fit.

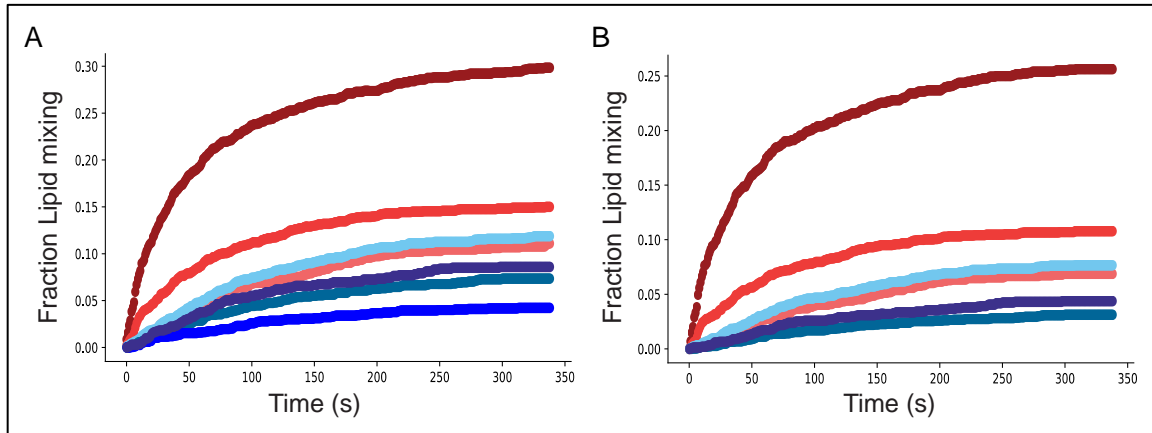
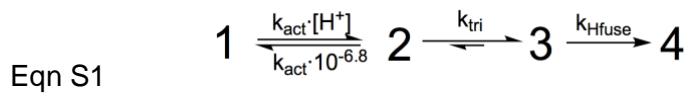


Figure S13. Background Correction of Hemifusion Kinetics The CDF at pH 7.4 (dark blue trace in panel A) was subtracted from the remaining CDFs to yield the corrected CDFs (panel B)

S3. Cellular Automaton Model

Cellular automata are a class of discrete spatial models which have been used to model spatial positioning and protein activation of viral proteins interacting with a target membrane during fusion^{4,11,12}. As described in the main text, we compared the conclusions of our kinetic modeling with a previous cellular automaton model⁴ of West Nile virus (WNV), a closely related flavivirus. This model was developed to describe single particle lipid mixing data similar to our Zika virus data, and utilized a variety of physical measurements, viral mutants, and previously known structural information of the viral E protein to define identities of intermediate states within the model. In the cellular automaton simulation, the E proteins at the interface between an individual virus and target membrane were modeled as a hexagonal array. Each E protein in the array could adopt 4 states during the simulation: 1) natively folded close to the viral membrane, 2) pH-activated, extended and inserted into target membrane, 3) in trimer with nearby extended partners, and 4) hemi-fused. This model can be written schematically as:



As written, this linear model is analogous to Equation (1) (main text), with the inclusion of one additional state. However, geometrical constraints were also implemented in the cellular automaton model, which are not captured by reaction schemes such as Equation (1) (main text). These geometrical constraints attempted to capture relevant spatial interactions between E proteins, and were implemented by allowing individual E protein monomers to adopt certain states in the model only by interacting with nearby partners. Consequently, E proteins could only trimerize (state 3) if two neighboring partners were also extended. Hemifusion (state 4) could only be achieved if a minimum number of neighboring trimers existed in the simulated interface. Additionally, E protein monomers were arranged in defined dimer pairs in state 1 to approximate the viral cryo-EM structure, and a measure of cooperativity within dimers was included for E protein extension.

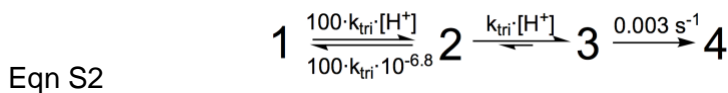
To run the cellular automaton model for a given pH value, many hundreds of virions were simulated, and the time between simulation start (pH drop) and hemifusion was measured for individual virions and compiled to construct distributions of waiting times, as were measured in the experiment. Before fitting the cellular automaton model to their WNV data, the authors used additional information to calculate some parameters. Notably, dynamic light scattering data of Kunjin virus (a WNV subtype) particles at various pH values was used to measure the equilibrium between E protein extension and retraction. Using this data, $k_{\text{ret}} = k_{\text{act}} \times 10^{-6.8}$, as shown in Eqn. S1. The authors then used this model to fit their West Nile virus lipid mixing data to determine $k_{\text{ext}} = k_{\text{act}} \times [\text{H}^+]$, k_{tri} , and the minimum number of trimers (N_{min}) needed for hemifusion, which they found to be 2.

In the main text, we demonstrated that linear models such as Equation (1) (main text) are insufficient to describe our Zika virus data (Figure S7 and Figure 4, main text). To determine whether the geometrical constraints in the cellular-automaton model could compensate for the absence of an off-pathway state, we re-implemented the WNV model and applied it to our Zika virus data, testing pre-equilibration and additional model states as described below to rigorously test the quantitative ability of this model to describe our multi-pH data. We assessed the fit of various formulations of the model, either with or without an off-pathway state, to our data.

Prior to performing these fits, we estimated k_{Hfuse} by fitting our experimental data at pH 4.6 to the cellular automaton model as shown in Equation (S1), only allowing k_{Hfuse} to vary, and keeping k_{ext} and $k_{\text{tri}} \gg k_{\text{Hfuse}}$. This fit yielded $k_{\text{Hfuse}} = 0.003 \text{ s}^{-1}$ and is the analogous procedure to our estimation of k_{AF} in the kinetic modeling section used in the single parameter fit. We used this value of k_{Hfuse} for all subsequent fits.

We then fit our entire experimental data set to the WNV model as described above, only allowing k_{act} and k_{tri} to vary, and otherwise using all other parameters as written in Equation (S1), including $N_{\text{min}} = 2$. The start state of the simulation can be an important determinant of the outcome. We allowed the E-protein monomers to equilibrate between the retracted and extended states at pH 7.4, and used this equilibrated state as our starting state. This pre-equilibration simulates the isolated virus in the absence of target membrane, and assumes that all other states in the model are target-membrane dependent. Fitting this model to our data, we observed very poor agreement (Figure S14).

Next, informed by our previous kinetic modeling from the main text, we allowed k_{tri} to be pH-dependent, and defined $k_{\text{act}} = 100 \times k_{\text{tri}}$, as shown in Equation (S2). This would suggest that trimer formation is dependent on pH, for which there is some support based on trimerization of isolated WNV E protein ectodomains in liposome co-flotation assays⁴, but which we are not attempting to model quantitatively here.



Using Equation (S2), we again observed that there was poor agreement between the best-fit solution and our data, as was predicted by our kinetic modeling (Figure S15A).

Lastly, we implemented the model shown in Equation (S3), including an off-pathway state analogous to Equation (2) (main text), and only allowing k_{tri} to vary in the fit.

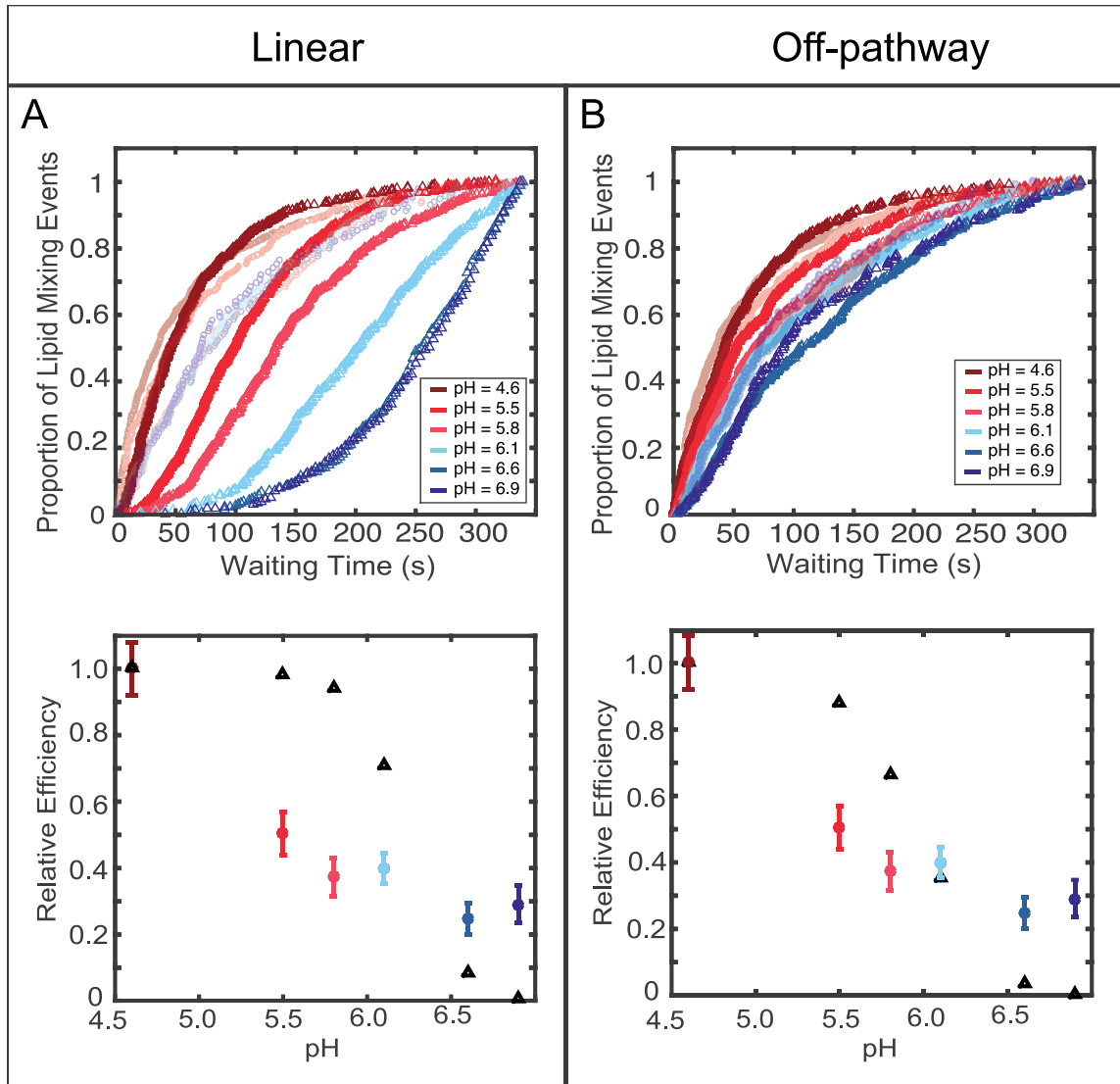


Figure S15. The addition of an off-pathway state to the cellular automaton models is necessary to describe both the experimental trends in the efficiencies and rates of single virus lipid mixing data. A one parameter fit of k_{tri} was performed on the linear model (Eqn. S2) (A) and the off-pathway model (Eqn. S3) (B) to fit our experimental data. The best fit rate constant was $k_{\text{tri}} = 2000 \text{ M}^{-1} \text{ s}^{-1}$ for the linear model (A) and $k_{\text{tri}} = 60000 \text{ M}^{-1} \text{ s}^{-1}$ for the off-pathway model (B). Rate constants: $k_{\text{ext}} = 100 \times k_{\text{tri}} \times [\text{H}^+]$; $k_{\text{ret}} = 100 \times k_{\text{tri}} \times 10^{-6.8} \text{ M}$; $k_{\text{tri}}' = k_{\text{tri}} \times [\text{H}^+]$; $k_{\text{O}} = k_{\text{tri}} \times 10^{-5.7} \text{ M}$, $k_{\text{Hfuse}} = 0.003 \text{ s}^{-1}$. triangles = model data, circles = experimental data.

S3.1 Effect of delay time between virus binding and pH drop on experimental hemifusion efficiencies

As discussed in the main text, a categorical shortcoming of both the kinetics and cellular automaton off-pathway models is that they would predict a strong dependence of the hemifusion efficiencies on the delay time between virus binding to the target membrane and the onset of pH drop. Presumably the off-pathway state is dependent on close proximity to a target membrane, else the native state of the virus would largely be in this off-pathway state. However, this would predict that the time window between virus binding and pH drop should be an important determinant of the extent to which the off-pathway state is populated at the start of our lipid mixing measurement. In preliminary data, we do not observe such a strong dependence (Figure S16). Roughly doubling the delay time between virus binding and pH drop did not significantly affect the relative hemifusion efficiencies.

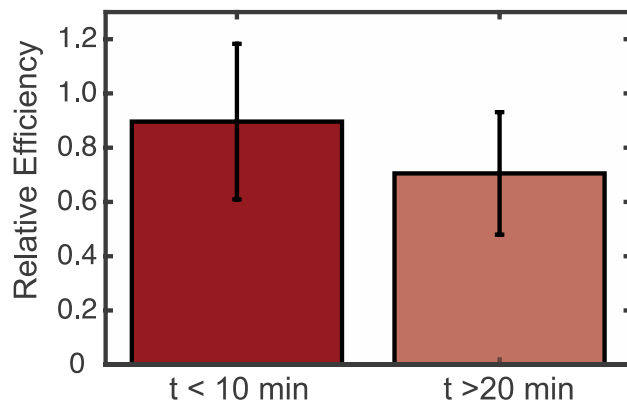


Figure S16. Doubling the delay time between virus binding and buffer exchange to low pH did not significantly affect the relative hemifusion efficiency. Virus was bound to vesicles, excess virus was rinsed, and the pH was lowered within 10 minutes or after 20 min. Relative hemifusion efficiency of the two conditions is within error indicating that these time windows do not significantly affect relative hemifusion efficiency.

S4. References:

- (1) Rawle, R. J.; Boxer, S. G.; Kasson, P. M. Disentangling viral membrane fusion from receptor binding using synthetic dna-lipid conjugates. *Biophys. J.* **2016**, *111*, 123–131, DOI: 10.1016/j.bpj.2016.05.048.
- (2) Chan, Y.-H. M.; Van Lengerich, B.; Boxer, S. G. Lipid-anchored dna mediates vesicle fusion as observed by lipid and content mixing. *Biointerphases* **2008**, *3*, DOI: 10.1116/1.2889062.
- (3) Hughes, L. D.; Rawle, R. J.; Boxer, S. G. Choose your label wisely: water-soluble fluorophores often interact with lipid bilayers. *PLoS One* **2014**, *9*, e87649, DOI: 10.1371/journal.pone.0087649.
- (4) Chao, L. H.; Klein, D. E.; Schmidt, A. G.; Peña, J. M.; Harrison, S. C. Sequential conformational rearrangements in flavivirus membrane fusion. *Elife* **2014**, *3*, DOI: 10.7554/eLife.04389.001.
- (5) Jones, M. C. Simple boundary correction for density estimation kernel. *Stat. Comput.* **1993**, *3*, 135–146.
- (6) Chan, Y.-H. M.; Lenz, P.; Boxer, S. G. Kinetics of dna-mediated docking reactions between vesicles tethered to supported lipid bilayers. *Proc. Natl. Acad. Sci. U. S. A.* **2007**, *104*, 18913–18918, DOI: 10.1073/pnas.0706114104.
- (7) Dowd, K. A.; Jost, C. A.; Durbin, A. P.; Whitehead, S. S.; Pierson, T. C. A dynamic landscape for antibody binding modulates antibody-mediated neutralization of west nile virus. *PLoS Pathog.* **2011**, *7*, e1002111, DOI: 10.1371/journal.ppat.1002111.
- (8) Austin, S. K.; Dowd, K. A.; Shrestha, B.; Nelson, C. A.; Edeling, M. A.; Johnson, S.; Pierson, T. C.; Diamond, M. S.; Fremont, D. H. Structural basis of differential neutralization of denv-1 genotypes by an antibody that recognizes a cryptic epitope. *PLoS Pathog.* **2012**, *8*, e1002930, DOI: 10.1371/journal.ppat.1002930.
- (9) Sabo, M. C.; Luca, V. C.; Ray, S. C.; Bukh, J.; Fremont, D. H.; Diamond, M. S. Hepatitis c virus epitope exposure and neutralization by antibodies is affected by time and temperature. *Virology* **2012**, *422*, 174–184, DOI: 10.1016/j.virol.2011.10.023.
- (10) Delvecchio, R.; Higa, L. M.; Pezzuto, P.; Valadão, A. L.; Garcez, P. P.; Monteiro, F. L.; Loiola, E. C.; Dias, A. A.; Silva, F. J. M.; Aliota, M. T.; et al. Chloroquine, an endocytosis blocking agent, inhibits zika virus infection in different cell models. *Viruses* **2016**, *8*, DOI: 10.3390/v8120322.
- (11) Ivanovic, T.; Choi, J. L.; Whelan, S. P.; Van Oijen, A. M.; Harrison, S. C. Influenza-virus membrane fusion by cooperative fold-back of stochastically induced hemagglutinin intermediates. *Elife* **2013**, *2*, DOI: 10.7554/eLife.00333.001.
- (12) Kim, I. S.; Jenni, S.; Stanifer, M. L.; Roth, E.; Whelan, S. P. J.; Van Oijen, A. M.; Harrison, S. C.; Brunger, A. T.; Hughson, F. M. Mechanism of membrane fusion induced by vesicular stomatitis virus g protein. *Prot. Natl. Acad. Sci. USA* **2017**, *114*, 28–36, DOI: 10.1073/pnas.1618883114.